HYDRODYNAMIC ANALYSIS OF THE WAVE BRIDGE CONCEPT

A THESIS SUBMITTED TO THE GRADUATION DIVISION OF THE UNIVERSITY OF HAWAIʻI AT MĀNOA IN PARTIAL FULFILLMENT OF THE REQUIREMENTS FOR THE DEGREE OF

MASTER OF SCIENCE

IN

MECHANICAL ENGINEERING

AUGUST 2016

by

Nelson Anthony Ikaika Fernandez

Thesis Committee:
Reza Ghorbani, Chairperson
Michelle Teng
Scott Miller

ACKNOWLEDGEMENTS

This project was possible due to the innovative thinking of my advisor, Dr. Reza Ghorbani. Dr. Ghorbani has given me a great project and many opportunities I will always be thankful for. The success of this project at MARIN is entirely the result of the tireless support and mentoring of my MARIN supervisor, Mr. Sebastien Gueydon. I would like to thank my committee members Dr. Michelle Teng and Dr. Scott Miller, for their support, guidance, and patience while I worked though my thesis. I would also like to thank my wife, Kanohokuahiwi, and two sons, Iminoelo and Kealaula, for letting me travel half way around the world to conduct this work and for providing a reason to always better myself and complete this thesis. I will be always grateful for their support.

Abstract

The Wave Bridge concept is a novel technology for mitigating primary floating platform displacements and nacelle accelerations of a Floating Wind Turbine (FWT) system by pursuing a radical departure from current traditional research in the field of FWTs. The study's objective was to determine if performance improvement was achieved by implementing the Wave Bridge concept through the use a comprehensive computational model within a three dimensional, frequency domain based on linear wave theory. The performance change of the system was determined by the change in nacelle accelerations since larger nacelle accelerations adversely affect FWT's operation lifetime, maintenance schedule, and power output. The study varied the Wave Bridge's body volume, separation distance, and incident angle to determine the dimensional effects of these parameters toward seeking optimization. Results show the relationship these dimensions contribute to performance improvements of 30% or performance degradations of 60%.

Table of Contents

List of Figures

List of Tables

List of Abbreviations and Symbols

A_R = Wave amplitude of radiating wave
A_{WL} = Waterplane Area
B = Damping
BBC: Bottom Boundary Condition
BEM: Boundary Element Method
BVP: Boundary Value Problem
b = Beam
CFSBC: Combined Free Surface Boundary Condition
C = Hydrostatic Restoring Force
D = Draft
FSDBC: Free Surface Dynamic Boundary Condition
FSKBC: Free Surface Kinematic Boundary Condition
FWT: Floating Wind Turbine
GM_L = Longitudinal Metacenter Height
GM_T = Transverse Metacenter Height
h = Water depth
k = Wave number
K = Radius of Gyration
KG = Location of CoG
L_{pp} = Length
n = Unit normal
RMS: Root-Mean-Square
TLP: Tension Leg Platform
V = Volume/Displacement
r = Radial distance from the body element
S = Separation Distance
Ψ = Percent Relative RMS Nacelle Acceleration
Φ = Velocity potential
Φ_D = Diffraction velocity potential
ϕ_I = Incident velocity potential
ϕ_R = Radiation velocity potential
θ - Angle of Inclined Wave Bridge Face
ω = Angular frequency
ζ = Free surface elevation at a chosen point

Chapter 1: Introduction

Motivation

Our understanding of floating structures' hydrodynamics has made much advancement from research by the oil and gas industry for fossil fuel exploration and production. Floating platforms were created because of their relatively low-cost for deep-sea tasks. There are many floating structure installations around the world with more added each year to keep pace with the world's demand for more fossil fuel-based products. In recent years, there has been a shifted focus toward the use of floating platforms for offshore wind turbines. In the 1970's, MIT's Heronemus shared the concept of offshore floating wind turbines (FWT) [Heronemus, 1972]. Heronemus' FWT ideas would mostly remain on the drawing board until the 1990's when the first major efforts would begin to be realized [Bulder *et al.*, 2002]

Current projects within the global wind energy industry include the London Array, Horns Rev, and Egmont an zee wind farms in the UK, Denmark, and Netherlands, respectively [Normark *et al.*, 2005]. However, these projects, like majority of the wind projects, utilize well-known technology through the use of bottom-mounted wind turbine platforms. These popular bottom-mounted structures are limited to locations no deeper than 35m [Cordle *et al.*, 2011]. Northern Europe is fortunate to have a relatively shallow continental shelf with depths no greater than 30m within 10-20km from shore for most of the coastal areas. However, many countries around the world wanting to develop their offshore wind resource infrastructure are unable to utilize bottom-mounted wind turbine products because seafloor depth is greater than 35m within 10 km. In these vast majority of cases, a floating wind turbine is the primary option.

Development of a resilient floating platform to survive years at sea is not a difficult task, nor is the development of a wind turbine to effectively extract wind energy from offshore wind

resources [Musial *et al.*, 2004]. Instead, it is the cost of a FWT system that is the largest obstacle in wide scale implementation. FWT technology will benefit from further research into tower-platform interaction and rotor-blade development without regard to noise restrictions; however, the deployment of a FWT system is heavily dependent on minimizing cost of production, cost of materials, and installation costs.

FWT platforms are unique in that they must be extremely economical in comparison to the cost of an oil and gas floating platform. Wind turbines have a lifespan of about 20 years [Musial *et al.*, 2006]. . The amount of energy, thereby income, FWT's can convert is dependent on weather. Therefore a floating platform must be effective in a wide range of sea states to maximize the lifetime power output. Cost and resilience are the two contradictory aspects that complicate the industrialization of many contemporary options.

Much of the research and technology developed for the oil and gas industry can in many ways be applied directly to floating offshore wind turbine concepts. Technologies like that of the Tension Leg Platforms (TLPs), spar-type platforms, the semi-submersible platform, and the barge-shaped vessel. The economics of such a concept continues to limit the floating wind turbine projects to the research and development phase. However, cost estimates in the 1990's proved floating wind turbines to cost three times that of onshore wind turbines and bottom-mounted systems to be twice that of the onshore counterparts. Bottom-mounted wind turbines today are now common throughout Europe; based on the progress of commercialization, it will not be long before floating wind turbines are commonplace throughout the world.

Pioneer companies, namely Hywind and FloatWind, are exploring the feasibility of deploying wind turbines on floating structures. Hywind is developing a spar floating platform

and FloatWind a semi-submersible type floating platform. These systems are much more complicated to analyze because the floating structures are free to move in six degree of freedom.

The concept of the Wave Bridge is entirely unique from current FWT research projects. This project examined the hydrodynamic properties of a separate structure around a FWT to absorb incident waves forward of the FWT before they impinge upon the floating structure, translate the energy through the Wave Bridge, and radiate waves aft of the floating platform. The aim of the concept is to minimize the wave induced motions of the platform and wind turbine.

Background and Literature Review

The fully coupled dynamic analysis of floating platform concepts, mooring systems, and the National Renewable Energy Laboratory's (NREL) baseline five megawatt wind turbine to determine the nacelle acceleration, platform displacement, and mooring system tensions was published by MIT researchers [Sclavounos *et al.*, 2007]. Sclavounos explored several thousand variations to yield optimized TLP and catenary models. Generally, the TLP designs required high mooring line tensions but yielded minimal Root-Mean–Square (RMS) nacelle acceleration. Conversely, the slack catenary lines resulted in minimal mooring line tension yet resulted in slightly higher RMS nacelle accelerations. In general, the pursuit of an optimized floating wind turbine system will require the compromise between minimized nacelle accelerations and mooring line tensions. The reason for this comprise is because the goal of this and similar research is the understanding of the response behavior of a FWT in various sea states. The Wave Bridge concept introduces a radical divergence from current research and traditional solutions where coupled, independent floating structures fore and aft of the FWT provide an alternative solution that can be applied to any FWT design, regardless of floating platform or mooring system design. Based on the literature review performed herein, while not absolutely exhaustive,

shows promise that this thesis project is the first-of-a-kind in terms of utilizing separate floating structures to create a sheltered volume for the FWT. The current research detailed within this thesis was a culmination of several previous projects, starting with the mathematical model develop by Wu for a two dimensional plunger-type wavemaker in a finite depth wave tank as shown in Figure 1 [Wu, 1988].

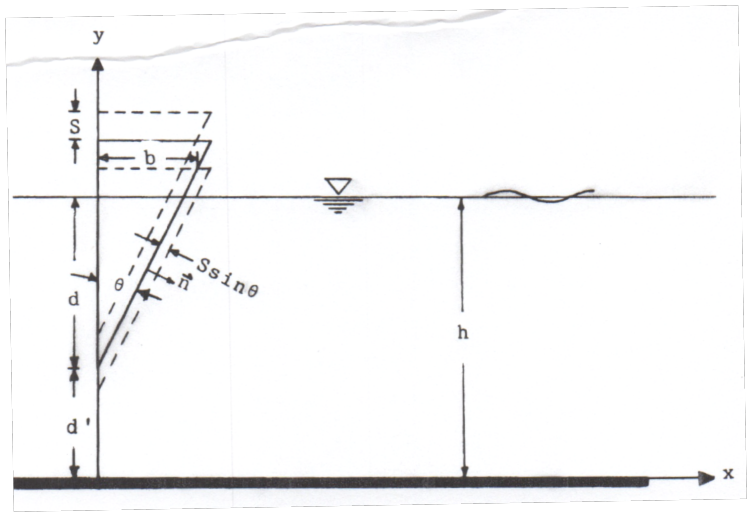

Figure 1: Illustration of the semi-analytical method developed for plunger-type wavemaker in a finite depth wave tank (from Wu, 1988).

In the 1988 Journal of Hydraulic Research paper, Dr. Yung-Chao Wu published his work on "Plunger-Type Wavemaker Theory" that explains a semi-analytical method to determine the characteristics of the radiated wave. This semi-analytical method is referred to as the boundary collocation method for solving the linear system of a two-dimensional plunger-type wavemaker in a finite depth wave tank. In 1988, computational power was limited so the semi-analytical approach reduces the need to perform large matrix operations resulting in a computation compact solution.

In 2011, following the works of Mei [Mei, 1976], Evans [Evan, 1976], and Newman [Newman, 1962] [Newman, 1977], Alam (Alam, 2010) sought to show the wedge plunger's

absorption efficiency potential through the radiation potential. It is widely accepted that in a 2D case, the absorption efficiency of a body can be determined if the radiation potential is known. Falnes [Falnes *et al.*, 1978] also echoes this remark by stating that a good wave absorber must be a good wave maker.

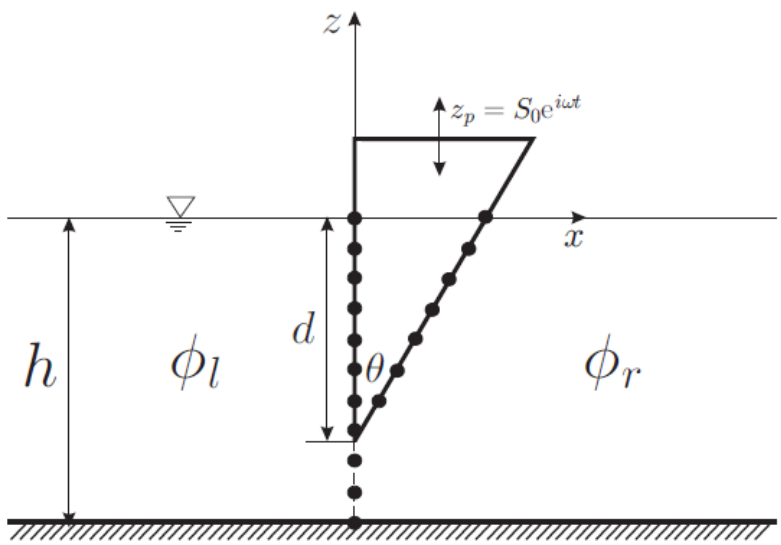

Figure 2: Illustration of a wedge shape wave maker with an aft radiation potential, ϕ_l and a forward radiation potential, ϕ_r (from Alam, 2010).

Alam's recent research, shown in Figure 2 and Figure 3, show the two analytical schemes used to determine the absorption efficiency of the two dimensional wedge shape wave energy absorber. In Figure 2, the aft radiation potential, ϕ_l and a forward radiation potential, ϕ_r are determined based on the periodic unit heaving oscillation of the wedge shaped wave maker. Intuitively, it is understood that the vertical face of the wedge shape wave maker will not radiate waves based on the inviscid fluid assumption of linear wave theory. In Figure 3, the aft velocity potential, ϕ_l and a forward velocity potential, ϕ_r are determined based the superposition of (1) a unit incident potential applied to the forward velocity potential region, (2) the resulting diffraction potential in both forward and aft potential regions, and (3) the forward and aft radiation potential shown in Figure 2.

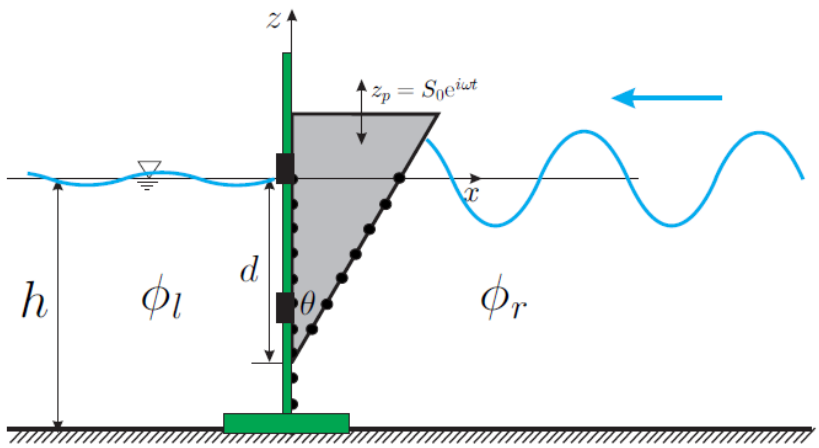

Figure 3: Illustration of a wedge shape wave energy absorber with an aft velocity potential, ϕ_l and a forward forawrd potential, ϕ_r where incident waves interact with the wave energy absorber and incident and diffracted wave energy is propagated left toward the aft region (from Alam, 2010).

The draft of this wedge shaped wave energy absorber is the primary variable affecting overall performance within this two dimensional model. If the ratio of depth to draft was unity, the plunger would be a wall separating the fluid domain into two separate regions. However, Figure 4, shows that when the draft, d, of the wave energy absorber is 70% of the water depth, h, the energy propagation from the forward velocity potential to the aft velocity potential allows left-travelling wave amplitudes to reach about 50% the height of right-going waves for long waves. The operational zone of a typical floating structure is 0.25-1.5 rad/s. In 300 m water depth this range equates to 0.08-3.15 on the x-axis of Figure 4. The survival zone is typically 0.25-1 rad/s. This means that only in rough weather and sea states will the system encounter such waves. This range equates to 0.2-3.0 on the x-axis in Figure 4. This range shows promise for an effective Wave Bridge with only a 10-20% draft-to-depth ratio. The difficulties of the current study is that not much is known for full-scale models and for the range λ/h = 0.0-1.0, which equates to $\omega \geq 0.45$ rad/s (majority of the typical diffraction test range of $0.0 \leq \omega \leq 3.0$)

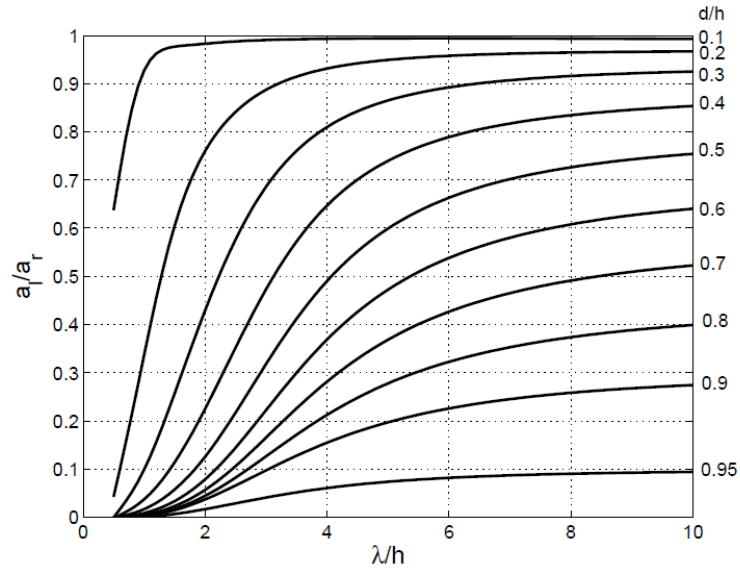

Figure 4: Results relating the ratios of wavelength to water depth (λ/h) and left-travelling wave amplitudes to right-travelling wave amplitudes (a_l/ a_r) along with trends at various water depths (d/h) (from Alam, 2010).

In 2012, Ghorbani, Alam, and Shakeri proposed the concept of a Wave Bridge for the use of sheltering floating bodies from the full effect of waves [Ghorbani *et al.*, 2012]. This project differs from many past and current research efforts because, unlike current research that seek to determine the optimal floating platform, wind turbine, and mooring coupled system design, this project looks to validate the notion that a floating platforms will benefit from the creation of a sheltered volume through the implementation of this Wave Bridge concept. The Wave Bridge concept, shown in Figure 5, utilizes two wedge-shaped bodies whose motions are coupled and considered to be one rigid body. The forward wedge-shaped body acts as a wave energy absorber and the aft wedge-shaped body acts a wave maker. The inclined faces of the bodies are facing outward from the protected volume. Thus, when an incoming wave induces a heaving motion in the forward wedge-shaped body the aft wedge heaves opposite thereby radiating a similar wave.

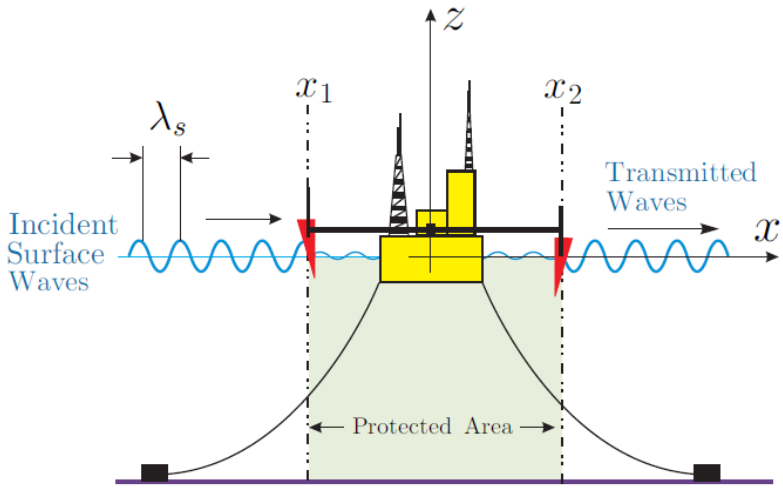

Figure 5: Illustration of Wave Bridge concept depicting the sheltered volume and the Wave Bridge that allows wave energy to bypass the floating structure

Objective

The main objective of this study is to evaluate the hydrodynamic characteristics of this Wave Bridge concept and determine the effects the incident wave angle, Wave Bridge width, and the separation distance of the two Wave Bridge bodies have on the hydrodynamic performance of the Spar floating platform. This goal is accomplished by comparing the Response Amplitude Operators (RAOs) of a solitary Spar floating platform and the RAOs of the combined Wave Bridge and Spar system to determine the effects of the body-body interactions.

The hydrodynamic analysis performed within this project concentrated solely on the underwater geometries of the Spar and Wave Bridge and the effects of incident, diffracted, and radiated waves on these configurations.

Chapter 2: Dynamics of the Floating Platform

Introduction

In this chapter the governing equations of hydrodynamic responses of floating structures are discussed. Comprehension of the theory of the diffraction calculations was essential to determining valid solutions for the application of MARIN's DIFFRAC hydrodynamics software for this unique study. Linear wave theory is assumed adequate for defining the problem and applied to the computational domain.

Directional Convention

The Wave Bridge and Spar's dynamics follow industry convention for defining the degrees of freedom. The x-axis runs from the vessels stern to bow, the y-axis from keel to deck, and the z-axis from port to starboard. There are six degrees of freedom for a body and are defined in detail in Table 1 below.

Table 1: Directional Convention

Numeric Designation	Name	Orientation	Mathematical Notation Convention
1	Surge	X-axis	X_1
2	Heave	Y-axis	X_2
3	Sway	Z-axis	X_3
4	Roll	Rotation about X-axis	X_4
5	Yaw	Rotation about Y-axis	X_5
6	Pitch	Rotation about Z-axis	X_6

Summation notation is used for the following equations. For the use of indices to define the cause and effect directs, such as added mass (A_{ij}) or damping (B_{ij}), the first index (i) denotes the mode affecting the body and the second index (j) denotes the reacting mode.

Boundary Value Problem (BVP) of Surface Waves

The fluid of the domain can be expressed a boundary value problem. The fluid is assumed to be irrotational and incompressible such that the Laplace equation is valid to define the velocity potential of the domain.

$$\nabla^2 \phi_j = 0 \qquad \text{(Eq. 2.1)}$$

where Φ is the velocity potential and j (= 0-7) denoted the appropriate velocity potential (j = 0, incident velocity potential; j=1-6, radiation velocity potential; and j = 7, diffraction velocity potential). Additionally the domain is assumed very large in the horizontal directions (x-z plane is very large) and the mean free surface is at y=0.

Boundary conditions are imposed upon the domain in order to solve the BVP. There are five boundary conditions considered. The BBC is given by a smooth, horizontal, impermeable seabed.

$$\phi_{j,x_2} = 0 \quad for: X_2 = -h \qquad \text{(Eq. 2.2)}$$

The free surface is defined by two conditions. One condition is the FSDBC that defines pressure at the surface to be that of atmospheric pressure. The second condition is the Free Surface Kinematic Boundary Condition (FSKBC) that defines the position of the fluid particle on the surface. These two conditions are often represented as the Combined Free Surface Boundary Condition (CFSBC).

$$g\phi_{j,x_2} - \omega\phi_j = 0 \quad for: X_2 = 0 \qquad \text{(Eq. 2.3)}$$

The bodies of the FWT platform submerged volume(s) are defined by the Body Boundary Condition. The condition defines the velocity of the fluid at the surface of the body is equal to the velocity of the body.

$$\phi_{j,n} = n_j \qquad \text{(Eq. 2.4)}$$

The last condition to satisfy is the Radiation Condition. This condition defines the wave amplitude in the far-field, an important factor since it was defined that this domain is very large. This condition defines the wave amplitude at r = ∞ distance from the body is equal to zero and wave amplitude decays exponentially from the body.

$$\lim_{r\to\infty}\left\{\sqrt{r}\left[\frac{\partial}{\partial r}\pm ik\right]\phi\ \right\}=0 \qquad \text{(Eq. 2.5)}$$

Linear surface waves are further defined by the dispersion relation which relates the angular frequency of the wave to the wave number such that

$$\omega^2 = \mathrm{k}\cdot\mathrm{g}\cdot\tanh kh \qquad \text{(Eq. 2.6)}$$

Diffraction and Radiation Theory

The mathematical model defined in the previous section describes a linear velocity potential, Φ, that describes all points in the domain. This velocity potential can be decomposed into three separate velocity potentials, the incident, diffraction, and radiation velocity potentials, such that

$$\phi = \phi_I + \phi_D + \phi_R \qquad \text{(Eq. 2.7)}$$

where their linear nature allows for the simple addition of these separate velocity potentials. The radiation velocity potential can be further decomposed such that the individual modes of motion possess their own velocity potential such that

$$\phi_R = \sum_{m=1}^{M}\sum_{j=1}^{6}\phi_j \qquad \text{(Eq. 2.8)}$$

where *j* represents the six modes of motions and *m* is the number of bodies in the scenario.

The diffraction velocity potential is the reflection of the incident wave off the body's wetted surface. Hence, the panel method is used to descretize the body's surface. At a given panel the incident body is reflected with respect to the orientation of the panel such that

$$\frac{\partial \phi_D}{\partial n} = -\frac{\partial \phi_I}{\partial n}, for\ j = 1,2,3 \qquad \text{(Eq. 2.9)}$$

The radiation potential is calculated for each mode where unit amplitude is used for each mode.

$$\phi_{R,n} = -i\omega A_R\, \phi_j \qquad \text{(Eq. 2.10)}$$

where Φ_R is the time-independent velocity potential and j is the motion mode.

The solution to the incident velocity potential is inferred using the Laplace equation and the boundary conditions defined above when the problem is not in shallow water and the water depth is constant.

$$\phi_I = \mathrm{Re}\left[\frac{-g\zeta}{\omega}\frac{\cosh k(X_2 + h)}{\cosh(kh)}\right] \qquad \text{(Eq. 2.11)}$$

The solution to the diffraction and radiation problems must be solved on a case-by-case basis since the solution includes the Body Boundary Condition. The diffraction BVP is summarized below:

$$\nabla^2 \phi_D = 0 \qquad in\ the\ fluid: X_2 < 0 \qquad \text{(Eq. 2.12)}$$

$$g\phi_{D,x_2} - \omega\phi_D = 0 \qquad on\ the\ free\ surface: X_2 = 0 \qquad \text{(Eq. 2.13)}$$

$$\phi_{D,x_2} = 0 \qquad on\ the\ seabed: X_2 = -h \qquad \text{(Eq. 2.14)}$$

$$\frac{\partial \phi_D}{\partial n} = -\frac{\partial \phi_I}{\partial n}, for\ j = 1,2,3 \qquad on\ the\ body\ surface \qquad \text{(Eq. 2.15)}$$

$$\lim_{r\to\infty}\left\{\sqrt{r}\left[\frac{\partial}{\partial r} \pm ik\right]\phi_D\right\} = 0 \qquad Radiation\ Condition \qquad \text{(Eq. 2.16)}$$

The radiation BVP is summarized below:

$$\nabla^2\phi_R = 0 \qquad in\ the\ fluid: X_2 < 0 \qquad \text{(Eq. 2.17)}$$

$$g\phi_{R,x_2} - \omega\phi_R = 0 \qquad on\ the\ free\ surface: X_2 = 0 \qquad \text{(Eq. 2.18)}$$

$$\phi_{R,x_2} = 0 \qquad on\ the\ seabed: X_2 = -h \qquad \text{(Eq. 2.19)}$$

$$\frac{\partial\phi_j}{\partial n} = -i\omega n_j \qquad on\ the\ body\ surface \text{ for j } = 1,2,3 \qquad \text{(Eq. 2.20)}$$

$$\frac{\partial\phi_j}{\partial n} = -i\omega(r\times n)_{j-3} \qquad on\ the\ body\ surface \text{ for j } = 4,5,6 \qquad \text{(Eq. 2.21)}$$

$$\lim_{r\to\infty}\left\{\sqrt{\boldsymbol{r}}\left[\frac{\partial}{\partial r} \pm ik\right]\phi_R\right\} = 0 \qquad Radiation\ Condition \qquad \text{(Eq. 2.22)}$$

Boundary Element Method

The Boundary Element Method (BEM) is the appropriate method to solve the BVP of the velocity potential about floating bodies since the domain is very large for real-scale models. BEM offers a computationally compact solver that solves the velocity potential along the boundaries by utilizing a source distribution technique to account for the interaction of a body panel upon the remaining panels in the domain.

This section does not try to explain the theoretical framework of BEM or how it was applied in this study to yield results, which is beyond the scope. Instead, this section explains the concepts the author learned to ensure the computer program yielded practical and consistent results within the limitations of a first-order BEM solvers. The following section explains in detail the commercial solution that was used to solve the BVPs and justification for the applicability of the software for the unique cases encountered in the study.

BEM satisfies all the boundaries of the domain except the Body Boundary Condition because the body is unique to the scenario investigated. The Green's Second Identity defines the

relationship between the bounded fluid domain and the wetted surface of the submerged volume of the investigated body.

$$\iiint_V (G\nabla^2\phi - \phi\nabla^2 G)dV = \iint_S \left(G\frac{\partial\phi}{\partial n} - \phi\frac{\partial G}{\partial n}\right)dS \qquad \text{(Eq. 2.23)}$$

where G is the Green function (a fundamental laplace operator solution to satisfy all of the boundary conditions, V is the fluid domain, dV is the boundary of the domain, S is the wetted surface of the investigated body, and ϕ is the exact solution for the velocity potential of the BVP.

For the BEM program, DIFFRAC and WAMIT are leading multi-body diffraction and radiation velocity potential solver programs. A research agreement between the University of Hawaii at Manoa (UHM) and the Marine Research Institute Netherlands (MARIN) allowed for access to DIFFRAC for a limited period to evaluate the applicability of DIFFRAC toward the non-traditional design of the Wave Bridge concept. In this study, DIFFRAC was applied to determine the fluid-body interaction solution of the multi-body scenarios.

Application of Governing Equations to Modeling the Wave Bridge Models

The MARIN 3D potential theory computer program, DIFFRAC, was used to solve the multi-body diffraction and radiation velocity potentials of the various Wave Bridge scenarios explored in this study. DIFFRAC also calculated the wave loads and corresponding motion responses of the freely floating and moored bodies under linear waves. DIFFRAC is an industry standard, much like WAMIT, and is used extensively by companies in the offshore industry, in many fields of research, and academia. MARIN has validated the program against many in-house physical model tests utilizing their extensive resources, decades of hydrodynamics experience, and world-class facilities in Wageningen, Netherlands.

DIFFRAC is a frequency-domain program, solving the time-independent velocity potentials (defined in the previous sections) at discrete incident wave frequencies over a specified range in regular frequency increments. The program utilizes the bodies' discretized geometry, center of gravity, radii of inertia about the three axes, and water depth. The body damping coefficients and added mass coefficients due to fluid-body interactions, which are frequency-dependent, are determined along with the velocity potentials. These parameters are applied with the bodies' dynamic characteristics to yield the motion response and normalized RAOs. It is the nacelle acceleration RAOs (X_1, X_2, and X_3 directions) of the various scenarios that are analyzed and compared against each other to quantify relative changes amongst the geometric variations.

Methodology

In order to properly compare the results of the numerous scenarios, the sole metric of performance of the Wave Bridge design is the Percent Relative RMS Nacelle Acceleration [Ψ], expressed as

$$\Psi = \frac{\mathrm{RMS}\left[a_{X_1,nac}, a_{X_2,nac}, a_{X_3,nac}\right]_{Spar\&WB} - \mathrm{RMS}\left[a_{X_1,nac}, a_{X_2,nac}, a_{X_3,nac}\right]_{Spar}}{\mathrm{RMS}\left[a_{X_1,nac}, a_{X_2,nac}, a_{X_3,nac}\right]_{Spar}} \circ 100\% \qquad \text{(Eq. 2.24)}$$

where $a_{X_1,nac}, a_{X_2,nac}, a_{X_3,nac}$ are the nacelle acceleration RAOs [m/s^2/m] in the X_1-, X_2-, and X_3-directions, respectively. These values are treated as an array and the RMS of the array is determined. The nacelle acceleration TF is the acceleration of the nacelle [m/s^2] per meter of incident wave. In practical terms, the Spar will roll and pitch as a result of a given wave field. The nacelle acceleration TF identifies the peak acceleration of the nacelle due to a one meter perodic, regular incident wave field at every wave frequency from 0.05 rad/s to 3.00 rad/s at 0.05 rad/s increments. The nacelle acceleration RAO as a result of a single solitary Spar is compared

to the Wave Bridge and Spar combination nacelle acceleration RAO. A negative Ψ refers to an overall performance improvement of the Spar as a result of the Wave Bridge concept. A positive Ψ refers to an overall performance degradation of the Spar as a result of the Wave Bridge concept.

The nacelle acceleration is a convenient metric to compare overall performance of a similar yet exceptionally complicated FWT systems and was first used by Sclavounos' research team [Sclavounos *et al.*, 2007]. Several recent studies [Sclavounos *et al.*, 2007], [Prowell, 2009], [EWEA, 2009] explain how useful the parameter of nacelle acceleration is for monitoring wind turbine lifetime, nacelle components' health, and effectively controlling power capture abilities. This single metric distills directional wave excitations and dynamic responses of a floating platform into a single value that can be used for back-of-the–envelope structural and lifetime calculations, and can even be used for ballpark calculations regarding wind power capture potential and efficiency. In the field of FWTs, nacelle accelerations are greatly augmented due to the motions of the floating platform. Unlike a bottom-mounted wind turbine where nacelle accelerations are purely the result of structural oscillations. As mentioned earlier in this thesis, there are no similar projects for further developing the methodology to perform experiments and compare results because this project deviates from traditional FWT research, hence hydrodynamic performance improvements are relative to the baseline solitary Spar floating platform.

It is of note that many of the previous research involved 2D heaving asymmetric bodies. Not much is known about the effects of additional modes of motion, nor particular Wave Bridge dimensions, nor optimal asymmetric geometries. Hence, the Wave Bridge concept was designed with generic dimensions to determine the relative performance of the study's

parameters (incident wave angle, Wave Bridge width, and the separation distance of the two Wave Bridge bodies). Previous numerical wave maker and preliminary numerical and experimental Wave Bridge results were for small scale models. Numerical work at MARIN with DIFFRAC allowed for full scale models and practical environmental conditions (i.e., depth).

The project will accomplish the objective through the performance of 3 separate studies. The baseline study of the Spar (Chapter 4) will establish the baseline hydrodynamic characteristics of the Spar. Implementation of the Wave Bridge concept is compared against the hydrodynamic responses of the Spar to quantify performance improvement. Study 1 (Chapter 5) evaluates a very wide Wave Bridge design using Body 1's geometry and the effects of separation distance of the Wave Bridge on the performance of the Spar. Study 1 includes 3 scenarios with separation distances of 20m, 50m, and 100m. Lastly, Study 2 (Chapter 6) evaluates a narrow Wave Bridge design using Body 2's geometry and the effects of separation and incident wave angle on the performance of the Spar. Study 2 includes 15 scenarios with separation distances of 20m, 40m, 60m, 80m, and 100m and incident wave angles of 0 degrees, 45 degrees, and 90 degrees.

This project does not explore some key issues. It does not attempt to determine a practical means of coupling the fore and aft sections of the Wave Bridge into a single rigid body nor does it explore the effects of the Wave Bridge coupled to the floating platform nor the effects of mooring a Wave Bridge. This model can be thought of as a moored spar with a single free-floating Wave Bridge deployed such that the submerged volumes was equidistantly fore and aft of the Spar floating platform.

Chapter 3: Design of Submerged Volumes

Introduction

In this chapter the design and implementation of the Wave Bridge and Spar are discussed. Design of the submerged volumes, primarily the discretization and meshing of the volumes, is of the utmost importance when using the BEM explained in Chapter 2. Points on the volume's surface must be collinear and coplanar (where applicable) as designed and panels must be properly specified to ensure no gaps between panels exist and that the nodes of a panel are appropriately and discreetly defined. The hydrostatic characteristics of the submerged volume must also be defined accurately, including such parameters as volume (V), radii of gyration ($K_{X_1X_1}, K_{X_2X_2}, K_{X_3X_3}$), hydrostatic restoring forces ($C_{X_2X_2}, C_{X_4X_4}, C_{X_6X_6}$), and more. This chapter defines the parameters used and the appropriate design criteria to ensure the volumes are compatible with DIFFRAC.

Wave Bridge

For this project the underwater geometry of a single Wave Bridge submerged volume can be considered to be a singular triangular prism of specific dimensions, as illustrated in Figure 6. The right triangular prism geometry was chosen it is asymmetric with a vertical face when oriented as shown in Figure 6. The idea of this asymmetric shape is essential for minimizing the radiated wave on the vertical face of the body.

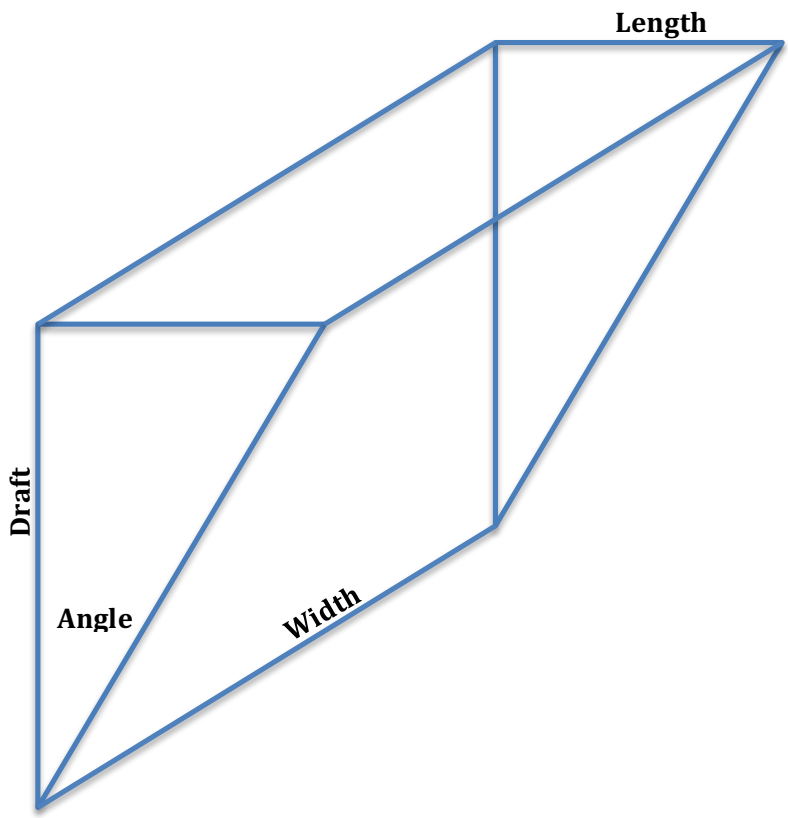

Figure 6: General dimensions of a single Wave Bridge submerged volume.

This triangular prism body is essentially a terminator–type, wedged-shaped wave energy absorber (or wave maker). The dimensions for the two body types can be seen below in Table 2.

Table 2: Triangular prism dimensions for the two bodies used in this study

Designation	Symbol	Units	Body 1	Body 2
Length	L_{pp}	m	30	17.32
Beam	b	m	74	20
Draft	T	m	51.96	30
Angle of the Incline Face	θ	deg	30	30
Waterplane Area	A_{WL}	m^2	4,400	692.8

Table 3 holds the relevant details of the three Wave Bridge configurations for Body 1. The Wave Bridge configurations refer to the two bodies separated by the specified distance. In

an earlier section the separation distance was defined as the distance between two vertical faces. In Table 3 the separation distance, D, is measured between the two vertical faces of the Wave Bridge bodies.

Table 3: Wave Bridge characteristics for Body 1

Designation	Symbol	Units	D = 20m	D = 50m	D = 100m
Displacement	V	m^3	118,238	118,238	118,238
Separation of CoG's	S	m	40	70	120
CoG fore of mid-ship	KG_X	m	0	0	0
CoG port of centerline	KG_Y	m	0	0	0
CoG above keel	KG_Z	m	41.31	41.31	41.31
Roll radius of gyration	k_{XX}	m	21.36	21.36	21.36
Pitch radius of gyration	k_{YY}	m	26.46	40.93	65.57
Yaw radius of gyration	k_{ZZ}	m	29.15	50.00	85.15
Heave hydrostatic restoring force	C_{33}	kN/m	44,645	44,645	44,645
Roll hydrostatic restoring force	C_{44}	kN-m/rad	12,640,348	12,640,348	12,640,348
Pitch hydrostatic restoring force	C_{55}	kN-m/rad	23,518,922	67,048,099	184,242,038
Transverse metacenter height	GM_T	m	10.90	10.90	10.90
Longitudinal metacenter height	GM_L	m	20.28	57.80	158.8

Table 4: Wave Bridge characteristics for Body 2

Designation	Symbol	Units	D = 20m	D = 40m	D = 60m	D = 80m	D = 100m
Displacement	V	m^3	10,391	10,391	10,391	10,391	10,391
Separation of CoG's	S	m	31.5	51.5	71.5	91.5	111.5
CoG fore of mid-ship	KG_X	m	0	0	0	0	0
CoG port of centerline	KG_Y	m	0	0	0	0	0
CoG above keel	KG_Z	m	20	20	20	20	20
Roll radius of gyration	k_{XX}	m	5.77	5.77	5.77	5.77	5.77
Pitch radius of gyration	k_{YY}	m	19.32	29.09	38.98	48.92	58.87
Yaw radius of gyration	k_{ZZ}	m	22.98	36.68	50.76	64.86	78.98
Heave hydrostatic restoring force	C_{33}	kN/m	6,966	6,966	6,966	6,966	6,966
Roll hydrostatic restoring force	C_{44}	kN-m/rad	232,202	232,202	232,202	232,202	232,202
Pitch hydrostatic restoring force	C_{55}	kN-m/rad	2,599,774	5,896,216	10,585,914	16,668,867	24,145,076
Transverse metacentre height	GM_T	m	2.22	2.22	2.22	2.22	2.22
Longitudinal metacenter height	GM_L	m	24.88	56.43	101.3	159.5	231.1

Spar

The spar-type floating platform is chosen over other floating platform options for two strong reasons. First, the adapted NREL/Hywind is well documented in terms of geometry, mass and spring characteristics, and the mooring system and wind turbine systems are well-defined. Second, the geometry is simple to model and can be meshed with a relatively simple mesh and still accurately define the geometry of the spar as opposed to more complicated designs, such as WindFloat. This simple mesh contributes greatly toward the reduction of computation time.

The key characteristics of the spar adapted from NREL OC3 reports are listed below in Table 5. The values for the radii of gyration and some additional properties were approximated iteratively to yield results similar to the NREL OC3 published results.

Table 5: Spar/Wind Turbine Characteristics [Jonkman, 2010][Gueydon *et al.*, 2011]

Designation	Symbol	Units	Spar
Waterplane area	A_{WL}	m^2	2200
Displacement	V	m^3	19,225
CoG fore of mid-ship	KG_X	m	0
CoG above keel	KG_Z	m	42
Roll radius of gyration	k_{XX}	m	48.39
Pitch radius of gyration	k_{YY}	m	48.39
Yaw radius of gyration	k_{ZZ}	m	4.91
Heave hydrostatic restoring force	C_{33}	kN/m	338.2
Roll hydrostatic restoring force	C_{44}	kN-m/rad	1,350,083
Pitch hydrostatic restoring force	C_{55}	kN-m/rad	1,350,083
Metacenter height	GM	m	17.053
Natural heave period (unmoored)	T_φ	s	30.6
Natural roll period (unmoored)	T_θ	s	28.5
Natural pitch period (unmoored)	T_Z	s	28.5

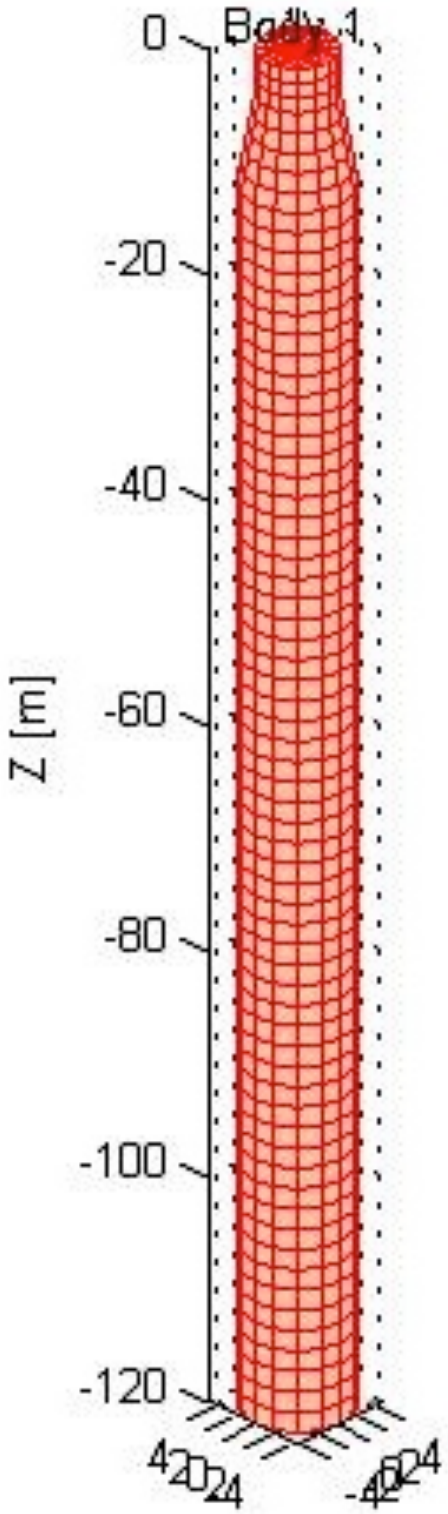

Figure 7. Spar Model

The hydrostatic restoring force was determined from published results. An additional spring matrix and linear damping matrix was included in LIFMOT to represent the mooring system and a 2% critical damping matrix was also included to account for any possible nonlinearities associated with the geometry. They are defined below.

$$C_{\text{added}} = \begin{pmatrix} 41.2 & 0 & 0 & 0 & 391 & 0 \\ 0 & 41.2 & 0 & -391 & 0 & 0 \\ 0 & 0 & 11.9 & 0 & -0.120 & 0 \\ 0 & -391 & 0 & 0.122\text{E}+06 & 0 & -4.00 \\ 391 & 0 & -0.120 & 0 & 0.122\text{E}+06 & 0 \\ 0 & 0 & 0 & -4.00 & 0 & 0.983\text{E}+05 \end{pmatrix}$$

$$B_{\text{Linear}} = \begin{pmatrix} 100 & 0 & 0 & 0 & 7.80\text{E}+03 & 0 \\ 0 & 100 & 0 & -7.80\text{E}+03 & 0 & 1.00 \\ 0 & 0 & 130 & 0 & -1.30 & 0 \\ 0 & -7.80\text{E}+03 & 0 & 6.08\text{E}+05 & 0 & -78.0 \\ 7.80\text{E}+03 & 0 & -1.30 & 0 & 6.08\text{E}+05 & 0 \\ 0 & 1.00 & 0 & -78.0 & 0 & 1.30\text{E}+04 \end{pmatrix}$$

$$B_{2\%\ \text{Critical}} = \begin{pmatrix} 32.8 & 0 & 0 & 0 & 285 & 0 \\ 0 & 32.8 & 0 & -302 & 0 & 1.00 \\ 0 & 0 & 68.2 & 0 & 0 & 0 \\ 0 & -302 & 0 & 2.63\text{E}+05 & 0 & -78.0 \\ 285 & 0 & 0 & 0 & 2.63\text{E}+05 & 0 \\ 0 & 1.00 & 0 & -78.0 & 0 & 5.53\text{E}+03 \end{pmatrix}$$

Mesh Analysis

The mesh of the spar and various wave bridge bodies were drafted and meshed in the computer aided design software, Rhinoceros 5, through the aid of proprietary MARIN plugins and compiled and converted in a MARIN MATLAB GUI called MATPAT that verifies the integrity of a mesh and exports the mesh into a PATRAN neutral file format compatible with DIFFRAC. Certain requirements must be met for DIFFRAC to work properly.

DIFFRAC panel requirements [7]:

- The panel characteristic length must be shorter than half the minimum wavelength.
- The use of panels with convex corners are preferred.
- The panels must have four points and four sides.
- The panel must be as square as possible, skew panels may yield inaccurate results.

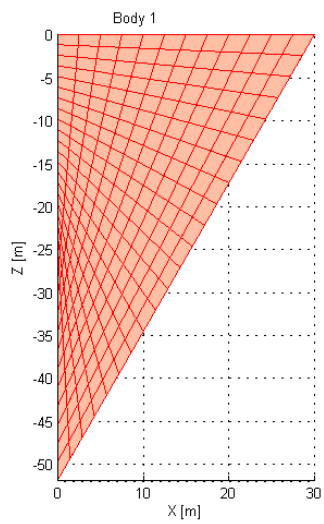

Figure 8. Example of the mesh used for DIFFRAC.

Figure 8 is an example of the mesh used in the DIFFRAC program. This side view shows a variety of quadrangular panels. Many panels are adequate in length and skewness. However, there are several panels, particularly in the middle of the vertical face that are no more

than slivers and can result in inaccurate results. The following sections will explain the mathematical method used to determine the mesh quality and the concluding remarks on the mesh quality used for this study.

Normal

The normal is essential for determining the pressure and force values acting upon the panels. The normals must point toward the fluid volume. It is calculated using the coordinates of the four points of an individual panel such that

$$N = (p_2 - p_0) \times (p_3 - p_1) \qquad \text{(Eq. 3.1)}$$

where p_0 is the first coordinate (x_{1_P0}, x_{2_P0}, x_{3_P0}) defined in the PATRAN file, p_1 is the second coordinate (x_{1_P1}, x_{2_P1}, x_{3_P1}) and so on.

Area

Accurately determining the area of each individual panel directly affects the accuracy of the results. Solving the BVP yields the pressure gradient throughout the domain. The pressure applied the a panel's area results in the wave forces acting upon our submerged volume, thereby affecting the RAOs of the Wave Bridge and Spar. Theoretically the area of a quadrilateral is trivial. However, in a discretized volume instead of calculating the area of the panel by the area of the plane defined by the four points, the area is instead defined as

$$A = \frac{1}{2}|N| \qquad \text{(Eq. 3.2)}$$

since the panel itself could possess torsion (i.e., all four points of a panel were not coplanar). The use of the panel's normal is unique because the units do not match on both sides of the equation. By an exhaustive inspection of arbitrary coplanar panels with in the mesh the equation held true. The characteristic length of the panel can then be found as the square root of half the

normalized normal. A table of the panels statistics of the mesh for the three triangular prism bodies and the spar are shown below in Table 6.

Table 6. Mesh area and characteristic length values for the three different wave bridge bodies and the spar

	Body 1	**Spar**
Minimum Area [m^2]	0.2025	0.1063
Maximum Area [m^2]	5.9834	6.1531
Average Area [m^2]	3.9425	3.7206
Minimum Length [m]	0.4500	0.3261
Maximum Length [m]	2.4461	2.4805
Average Length [m]	1.9759	1.9082

Skewness

The skewness of a mesh is a critical characteristic of meshes for DIFFRAC and most other numerical programs utilizing a panel method. The skewness is the quantified value of how similar a mesh panel is to ideal equilateral or equiangular triangle or square of itself.

Table 7. General Skewness Values [MARIN, 2011]

Value of Skewness	**Panel Quality**
1.00	Degenerate
0.90 – 1.00	Bad (Sliver)
0.75 – 0.90	Poor
0.50 – 0.75	Fair
0.25 – 0.50	Good
0.00 – 0.25	Excellent
0.00	Equilateral

The value "0" refers to a panel that is equilateral or equiangular. The value "1" refers to a panel that is degenerate and does not properly represent the geometry it is mean to represent. DIFFRAC only utilizes quadrangular meshes. A panel with skewness 1 does not immediately

cause concern, however, if enough panels of poor quality exist in the mesh than the results will surely be inaccurate. In this case the angles of the panel were used to calculate the skewness such that

$$skewness = MAX\left[\frac{\theta_{\max} - 90}{90}, \frac{90 - \theta_{\min}}{90}\right] \quad \text{(Eq. 3.3)}$$

where $\theta_{\max}$ is the maximum angle of the panel and $\theta_{\min}$ is the minimum angle of the panel and the values are calculated in degrees. The skewness characteristics for each body can be seen in Table 8.

Table 8. Mesh Skewness

	Body 1	**Body 2**	**Spar**
Minimum Skewness	0.0000	0.0000	0.0000
Maximum Skewness	1.0000	1.0000	1.0000
Average Skewness	0.0617	0.0658	0.0586

A statistical analysis all panels for each body show an average panel length of 1.90-1.98 m. The shortest wave (ω = 3.0 rad/s) has a wavelength of 6.85 m. By visual comparison of this wavelength with the values of Table 6, the average characteristic length of the panel is less than 1/3 the shortest wavelength. In fact, the maximum characteristic length of all the bodies are less than ½ the shortest wavelength, satisfying a panel length requirement for DIFFRAC. It can be seen in

Table 8 the average skewness is "excellent" based on the criteria in Table 7 and can be alternatively thought of as only ~6% of the panels are not fit for use in DIFFRAC. All bodies have panels that are ideal and panels that are degenerate. The meshes are statistically adequate to be used in DIFFRAC, the number of good panels are far more numerous than the number of degenerate panels.

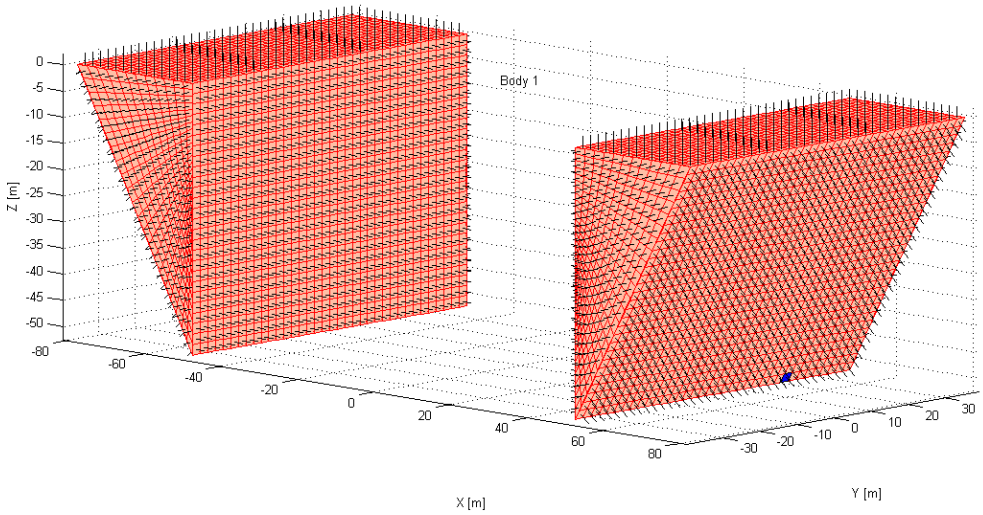

Figure 9. Example of the panels that experience the maximum velocities

Figure 9 is an example of the typical panel that experiences the highest velocities. The panel is highlighted in blue. The panels that experience the maximum velocities are determined in the .OUT file of the DIFFRAC package in DIFFRAC. These panels can occur on all ten faces of the Wave Bridge; however, something that all panels have in common is that the characteristic panel length and the skewness all satisfy the DIFFRAC requirements. This leads to the conclusion that numerical irregularities are not a result of the mesh, but instead due to the radiation problem of the Wave Bridge.

Chapter 4: Hydrodynamic Analysis of a Solitary Spar Floating Platform

Introduction

Obtaining an accurate baseline of the floating platform's dynamic responses is critical for use as a benchmark for evaluating the performance improvement or degradation of the Wave Bridge concept. The spar is geometrically similar to that of the Statoil Hywind spar, however, the dimensions of the spar more closely follows the NREL-modified spar for the OC3 project that utilizes the NREL benchmark 5-MW wind turbine, as further explained in Chapter 3.

The numerical model was determined using DIFFRAC and further processed using the LIFMOT package for dynamic responses, MATLAB for data manipulation and visualizations, and Neptune for 3D visualizations.

Several assumptions were applied to the numerical model. First, the spar floating platform is a rigid body. Second, linear wave theory, derived in Chapter 2, was applied to the entire numerical domain. Third, non-linear dynamics were ignored, including wave loads, viscous damping, mooring damping, etc. Lastly, the waves scenarios only consider head waves, neglecting quartering waves because the SPAR mesh was virtually symmetrical in the wave plane.

The *Result and Discussions* and *Summary* sections present the baseline case of a solitary spar floating platform and identify the important characteristics related to the motion RAO and nacelle accelerations.

Results and Discussion

As with all hydrodynamic analyses, the motion RAO of the spar was determined for the 6 DOF. These results are the baseline for spar motions used to compare in later cases involving the Wave Bridge's effects on the Spar. The resulting RAOs are plotted in Figure 10 with the

translation modes illustrated in the left column and the rotation modes illustrated in the right column. The translation modes' units for Figure 10 are "meter translation per meter of incident wave" or [m/m]. The rotation modes' units for Figure 10 are "radians rotation per meter of incident wave" or [rad/m].

The results for the motion RAO agree with general assumptions that in head waves the dominant modes of motion are heave and pitch with virtually no response occurring in the sway, roll, and yaw modes. Figure 10 shows a large magnitude response in the surge mode for the incident wave frequency 0.05 rad/s. This response is clearly outside the operation range of most floating platforms (0.8-2.0 rad/s) and is a result of the incident wave behaving as a shallow water wave in this water depth. Hence, linear wave theory is not valid for these very low frequencies and the surge response can be disregarded.

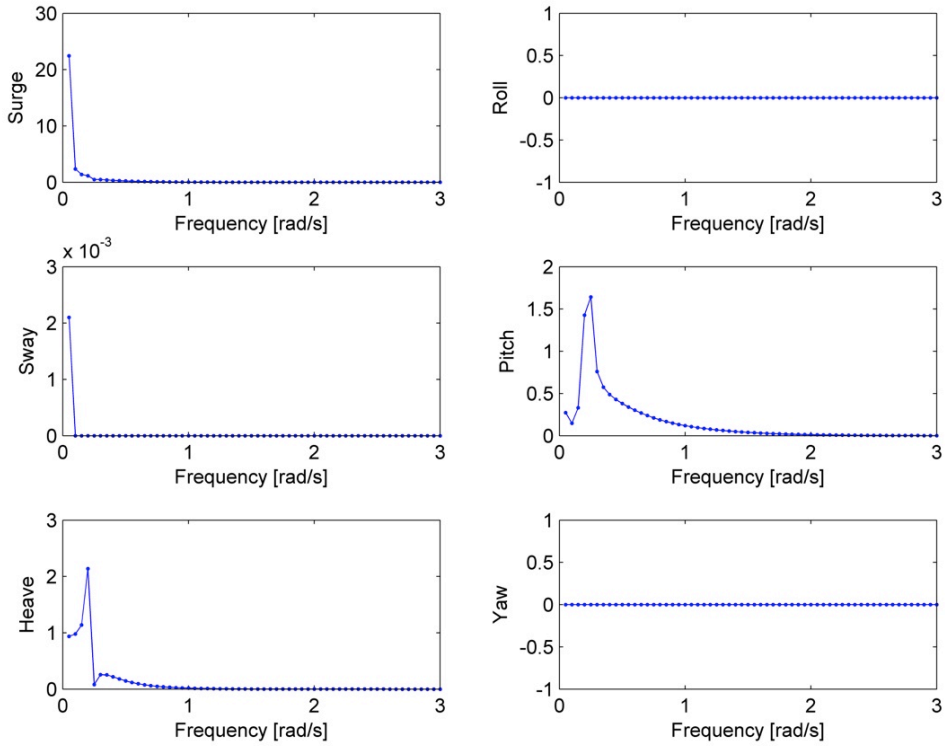

Figure 10. Baseline Motion RAO for the Spar Floating Platform

As mentioned above, heave and pitch are the dominant modes for this spar platform. Figure 11 plots the key parameters of the floating platform determined through the hydrodynamic analysis. The left column of the figure illustrates the excitation force, potential damping coefficient value, and motion RAO for heave. The right column illustrates the same parameters for pitch.

In the heave mode, the wave exerts a substantial force upon the spar floating platform. However, it is seen that spar's natural resonance (~0.2 rad/s) and anti-resonance frequencies (~0.25 rad/s) are very similar. At the point of anti-resonance, the heave RAO is virtually zero. At the point of resonance, the platform experiences its greatest motion regardless of the fact that the excitation force is less than three time the greatest heave force acting on the system. For the lower frequencies of incident wave the spar platform resembles the heave behavior of a buoy following the wave surface as evidenced by the heave RAO values near unity. After the anti-resonance frequency, the heave RAO is much smaller than unity due to the low water plane area to spar's mass.

The pitch RAO resonance frequency occurs at the heave anti-resonance frequency (0.25 rad/s). The magnitude for pitch motion is less than the heave mode but motion occurs for a wider wave spectrum as a result of the pitch excitation force occurring at a wider spectrum.

Hence, in order to improve the effectiveness of the Spar design, the Wave Bridge could provide hydrodynamic improvement by sheltering the spar from these excitation forces or perhaps capitalize on the anti-resonance phenomenon.

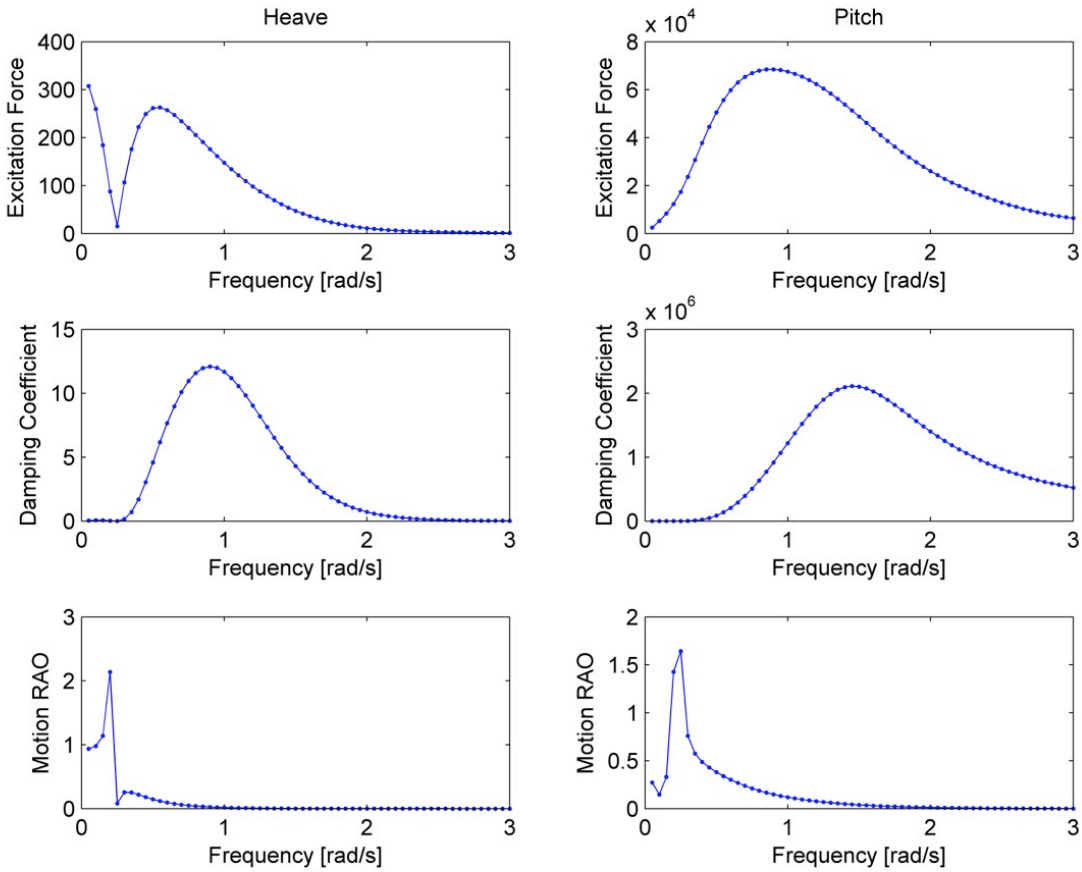

Figure 11. Heave and Pitch Characteristics for the Spar Floating Platform

The nacelle acceleration for the Spar floating platform is the primary performance index of system improvement for analyzing the impact of the Wave Bridge on the FWT system. The nacelle acceleration is related to turbine performance, equipment damage, and lifetime. Understanding nacelle kinematics provides a means for designing for low maintenance FWT.

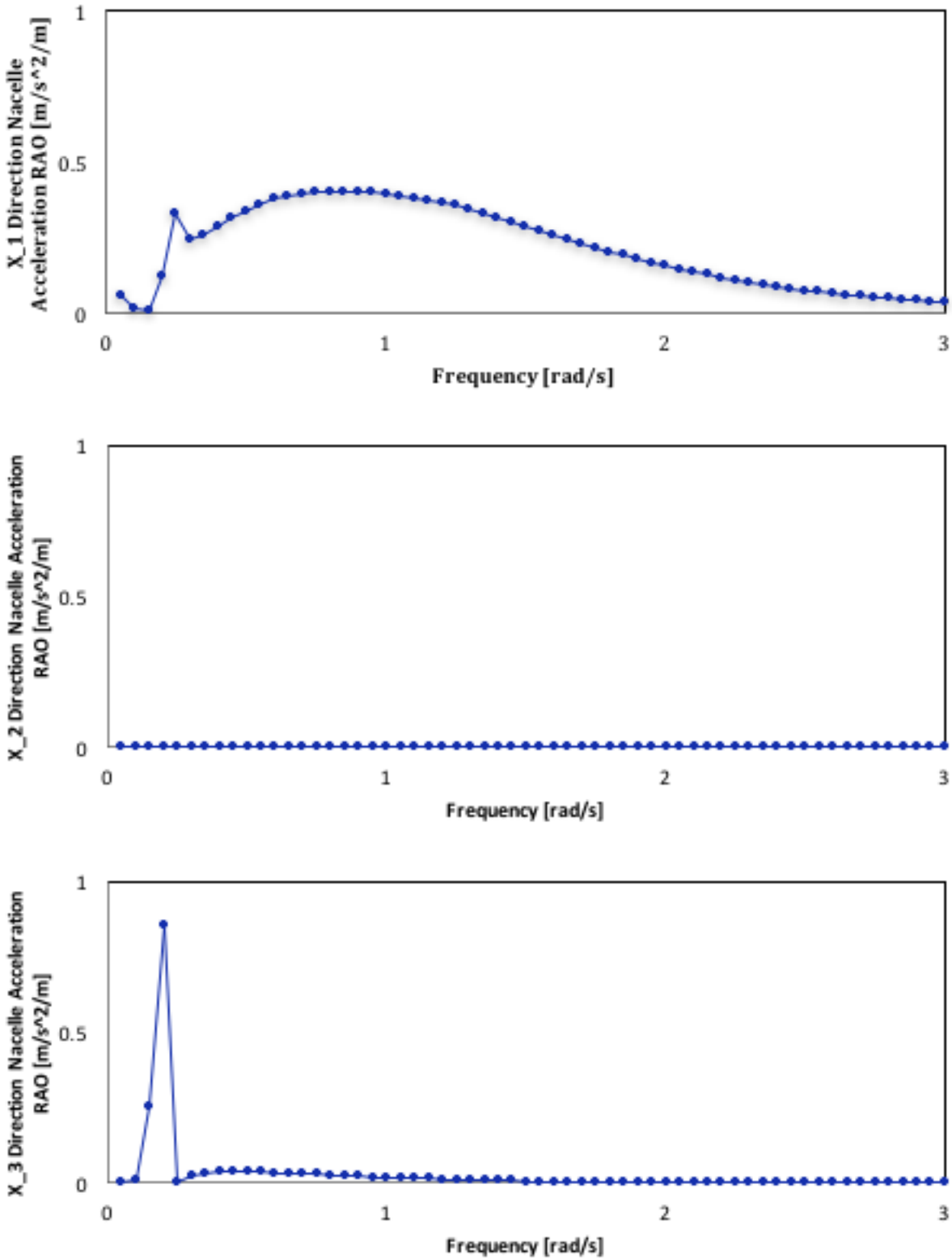

Figure 12. X_1-, X_2-, and X_3-direction Nacelle Accelerations for a Solitary Spar Floating Platform

The nacelle acceleration decomposed into the three Cartesian directions based on the vessel's coordinate system is shown in Figure 12. The nacelle experiences no lateral accelerations under head wave conditions. The nacelle does experience large magnitude x_3-direction (Heave) accelerations for a narrow spectrum (0.10 - 0.25 rad/s) as a result of the heave resonance frequency (around 0.20 rad/s as illustrated in Figure 11) and smaller magnitude x_1-direction accelerations for virtually the full spectrum of the numerical model as a result of the pitching motion of the Spar (as illustrated in Figure 11). It is important to clarify that the pitching mode (x_6-direction) of the Spar results in a surging acceleration of the nacelle (x_1-direction) and likewise the heaving mode (x_3-directiong) of the Spar results in a heaving acceleration of the nacelle (x_3-direction). Although the pitch response (shown in Figure 11) peaks at 0.25 rad/s and quickly diminishes in magnitude as the frequency increases, the surging acceleration steadily increases and does not peak until 0.85 rad/s where it steadily diminishes toward zero near the end of the frequency band. The increase in pitch frequency of the nacelle is greater than the decrease of pitch magnitude and causes a narrow spectrum pitch RAO to result in a broad spectrum x_1-direction nacelle acceleration RAO.

Additionally, virtually all the significant accelerations in the x_3-direction occur outside the operational spectrum and are of minimal concern and would cause minimum influence to an actual FWT. Consequentially, the x_1-direction accelerations are present for the full spectrum and are the primary concern of the Wave Bridge.

In order to utilize the nacelle acceleration RAOs presented in Figure 11 the RAOs are condensed into the RMS Nacelle accelerations by taking the RMS of the nacelle acceleration RAOs. Table 9 provides a summary of the RMS nacelle accelerations per incident wave height. The columns of Table 9 identify the different components of the nacelle acceleration (e.g., x_1, x_2,

and x_3-directions) along with the overall nacelle acceleration if the different modes were to be collapsed into a single scalar. The rows of Table 9 provide different ranges of incident wave frequencies (i.e,. perspectives). The first row is the full range of a wave frequencies calculated under each individual scenario. The full range is not arbitrary and is based on industry experience and used as a MARIN standard when evaluating the frequency domain of floating objects. The end points of 0.05 and 3.00 with increments of 0.05 provide an acceptable resolution to evaluate the hydrodynamics of floating object throughout a range of waves most likely to be encountered throughout the world. The normal operating range and rough water range are related to MARIN standards. Typically, a floating wind turbine is not expected to operate in waves outside the 0.80 – 2.00 rad/s range. The range of waves considered to be rough are 0.20 – 3.00 rad/s. However, this is a misnomer. A rough sea state is related to wave height. In this rough water range, rough sea states are likely to be formed and encountered.

Table 9. RMS Nacelle Acceleration Per Incident Wave Height for a Solitary Spar Floating Platform

	X_1–Direction [$m^2/s/m$]	**X_2–Direction [$m^2/s/m$]**	**X_3–Direction [$m^2/s/m$]**	**RMS Nacelle Acceleration [$m^2/s/m$]**
Full Range of Wave Frequencies (0.05 – 3.00 rad/s)	0.2549	0.0000	0.1163	0.1618
Normal Operating Range (0.80 – 2.00 rad/s)	0.3138	0.0000	0.0123	0.2081
Rough Water Range (0.20 – 3.00 rad/s)	0.2614	0.0000	0.1144	0.1647

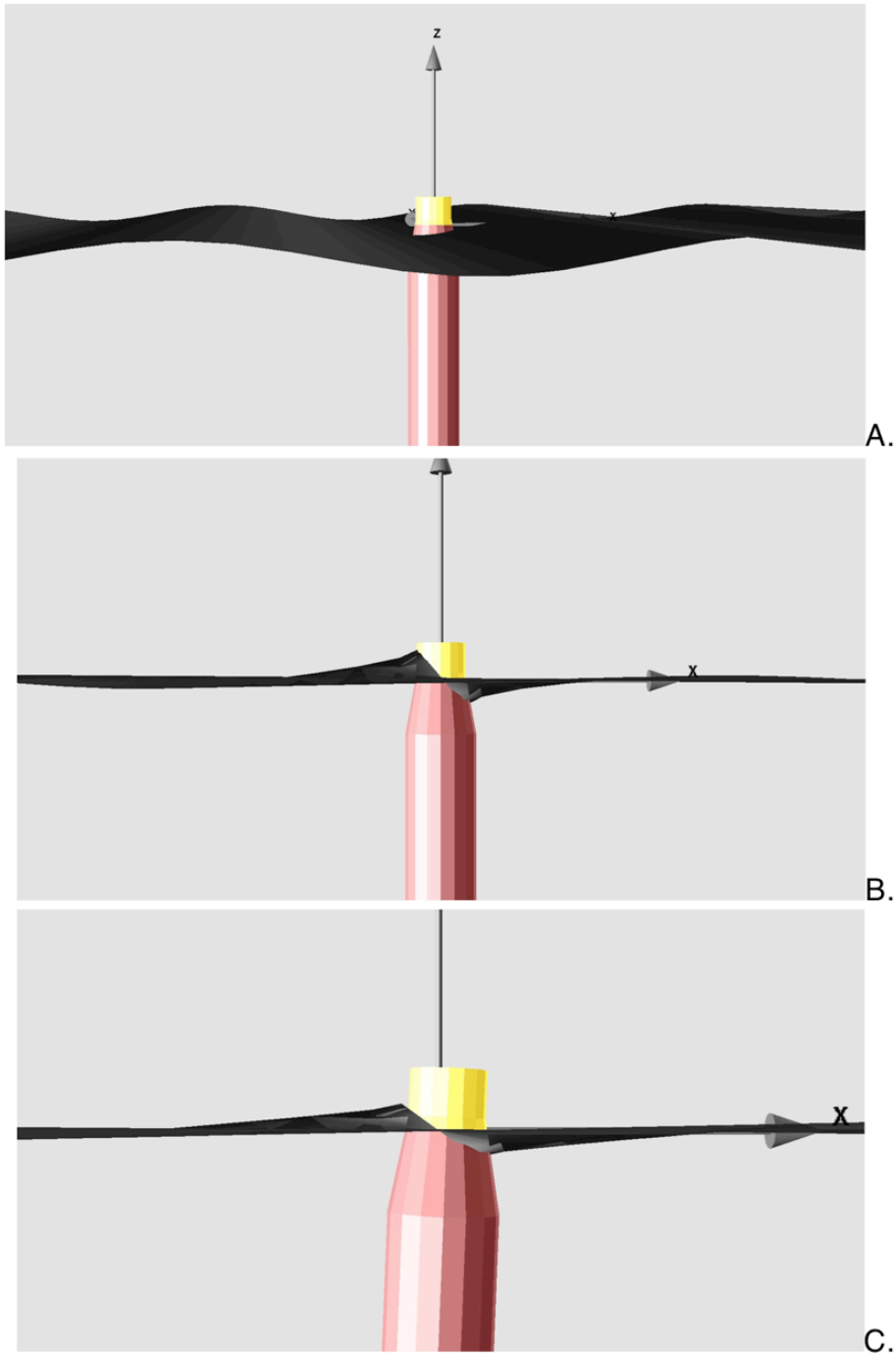

Figure 13. Neptune-generated time-domain wave field visualizations for waves with period, T=6.283 s (ω=1.0 rad/s). A) Incident waves, scaling factor = 2. B) Diffracted wave, scaling factor = 10. C) Radiated wave, scaling factor = 20.

Time Domain Visualization of the Spar

The final portion of evaluating the case of the independent Spar was the performance of a time domain visualization was performed to visually inspect the wave field and the motion responses of the spar. The MARIN-developed program, Neptune was used to visualize the system. Figure 13 illustrated the wave profile for the (A) incident waves, (B) diffracted waves, and (C) radiated waves whose velocity potentials were determined in DIFFRAC. The visualizations shown in Figure 13 were scaled to shown significant wave surface displacements. The incident, diffracted, and radiated waves were scaled up by a factor of 2, 10, and 20, respectively. Ultimately, the visualization of the Spar in a time-domain environment while attractive does not provide the level of detail obtained through the evaluation of frequency-domain data. Yet it is quite clear that the Spar geometry induces very minimal diffracted and radiated waves despite its nature to pitch and heave.

Chapter 6: Hydrodynamic Analysis of the Wave Bridge and Spar

Introduction

This chapter presents the data and results of 18 different scenarios that make up the Wave Bridge project for this thesis. These 18 scenarios are split into two main studies. The first study evaluates the effects of separation distance on the effectiveness of the Wave Bridge. This study utilizes the first three scenarios where we determine the Spar hydrodynamic responses when interacting with a Wave Bridge made up of two Body 1 volumes separated by 20m, 50m, and 100m. The second study, comprised of the remaining 15 scenarios, evaluates the effects of separation distance (with finer incremental increases) and incident wave angles on the Wave Bridge made up of two Body 2 volumes. The separation distances for the second study were 20m, 40m, 60m, 80m, and 100m and the incident angles are 0 degrees (head waves), 45 degrees (forward quartering waves), and 90 degrees (beam waves).

The Effects of Separation Distance of the Wave Bridge Bodies on the Hydrodynamic Performance of the Spar Floating Platform (Study 2)

The nacelle acceleration RAOs of the Spar are shown in Figure 14, Figure 15, and Figure 16 where the blue curve with circles at each data point is the results of the solitary Spar presented in Chapter 5 and the red curve with squares at each data point is the results of the Wave Bridge and Spar combination.

There are two glaring differences between the solitary Spar results and the Wave Bridge and Spar combination results that are common throughout the three scenarios. First, there are frequency ranges where the magnitude of the amplitude response is significantly smaller in the Wave Bridge and Spar combination than in the solitary Spar model. Second, there are seemingly random spikes in the Wave Bridge and Spar combination RAOs that are noticeably larger in

magnitude than the solitary Spar RAOs at certain frequencies and appear to be caused by an error in the numerical model, an error in post-processing of the data, or something else entirely.

The first difference is explained as the designed intent of the Wave Bridge concept. Based on 2D numerical models conducted at UC Berkeley (Alam, 2010) for asymmetrical plunger-type wave absorbers, it was shown that the wave heights of waves could be greatly reduced when the incident waves encounter the asymmetrical body. The Wave Bridge concept was born from a qualitative extrapolation of this computationally validated phenomenon. The Wave Bridge concept was further tested by informal laboratory experiments at the University of Hawaii at Manoa and the University of California-Berkeley. Both experiments involved a Wave Bridge model in a long flume to mimic a 2D environment. Although both experiments did not lead to published work it did provide the only empirical data available regarding the Wave Bridge concept prior to this thesis. Qualitative data from these experiments has shown that diffracted waves would leak energy beneath the Wave Bridge and affect the sheltered region. It was expected that the Wave Bridge concept had the potential to reduce the wave heights and thereby the Spar motions and accelerations. This is the performance improvement of the Spar as a direct result of the presence of the Wave Bridge. It was unknown how much the Wave Bridge affects the Spar. Figure 14, Figure 15, and Figure 16 quantify this effect.

The second difference was difficult to evaluate because there is not much precedence for these spikes in the RAOs. Although the nacelle acceleration RAOs is presented in Figure 14, Figure 15, and Figure 16 these spikes in the RAOs show up in all characteristics of the hydrodynamic model including the pitch and heave RAOs, the damping coefficient RAOs, the added mass RAOs, etc. Based on past MARIN research involving hydrodynamic responses of tanker vessels moored next to FSPO vessels (Floating Production Storage and Offlanding),

similar RAOs were encountered. An evaluation from these studies determined a computational error related to the boundary mesh size of the the free surface between the two vessels that are separated by several meters. This error was artificially rectified by inserting a Damping Lid at the free surface that would reduce the values at the free surface between the two vessels to values the were similar to those typically encountered during scale model experiments. This approach does not apply to the spikes. Further evaluation of the frequency- and time-domain results has determined the spikes are not errors but the result of a real change to the wave field as a result of the Wave Bridge. The large spikes are the results of standing waves within the protected region. The standing waves are produced as a result of the diffracted wave field around the leading body of the Wave Bridge. The diffracted waves then impinge upon the interior of the trailing body of the Wave Bridge. For some of the wave periods some energy is trapped and the wave travels within the Wave Bridge to create a standing wave. For example, the scenario of the 50m separation distance should cause standing waves if the waves are 100m, 50m, 16.67m, 12.5m, etc. The x_1-direction nacelle acceleration identifies peaks at 1.05 rad/s, 1.4 rad/s, 1.8 rad/s, 2.1 rad/s, 2.4 rad/s. The wavelength corresponding to these frequencies are 55.90m, 31.45m, 19.02m, 13.96m, and 10.70m.

The last major characteristic to observe is the change in the x_3-direction RAOs as a result of the standing waves. The natural frequency spike of the solitary Spar scenario is diminished by the Wave Bridge. However, the standing wave induced acceleration spikes are now present as a result of the Wave Bridge. Yet, the orders of magnitude of the heave accelerations do not cause specific concern when compared to the pitch accelerations.

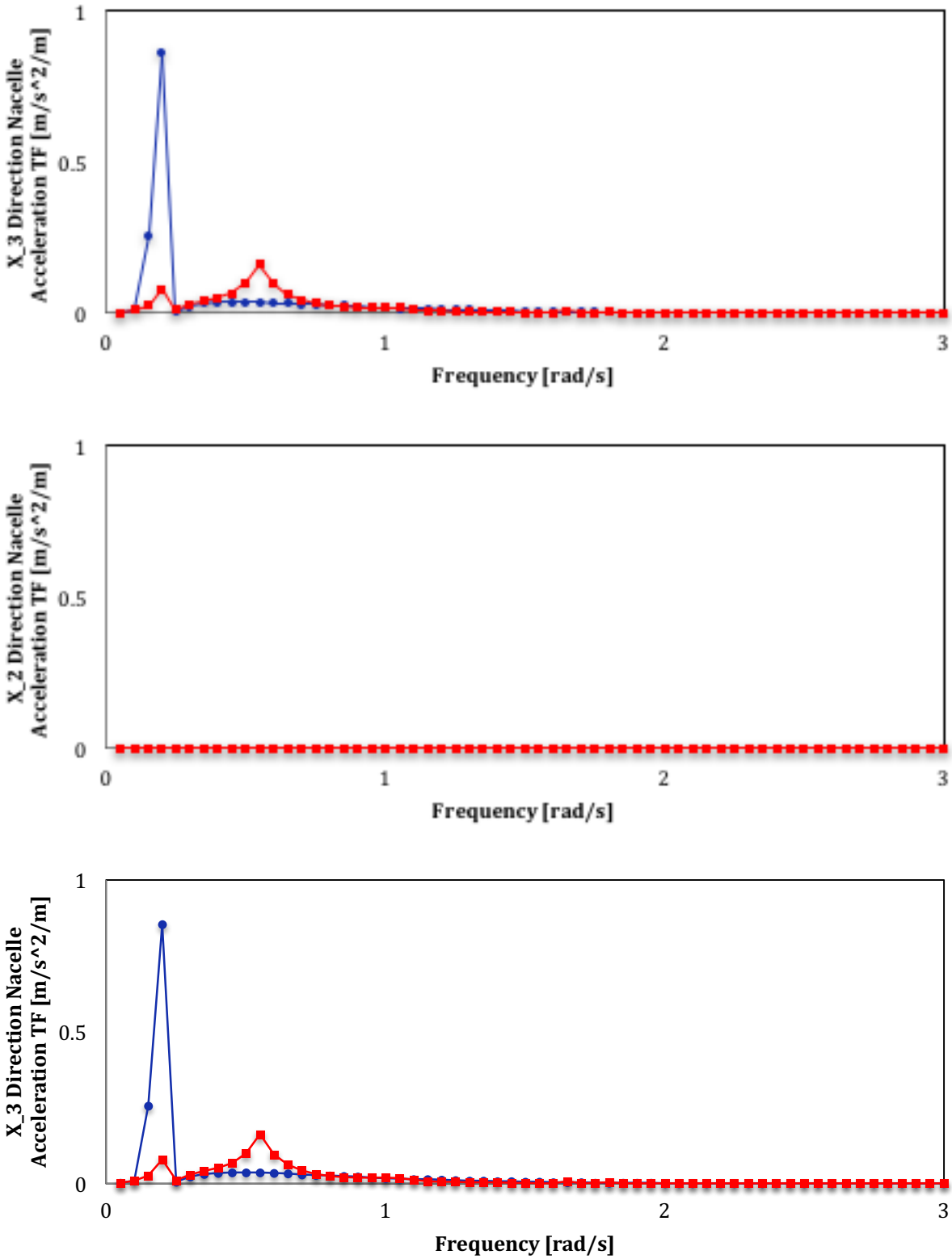

Figure 14. X_1-, X_2-, and X_3-direction Nacelle Accelerations for the Solitary Spar (Blue/Circle) and Spar/Wave Bridge (Body 1, S = 20m, Scenario) (Red/Square)

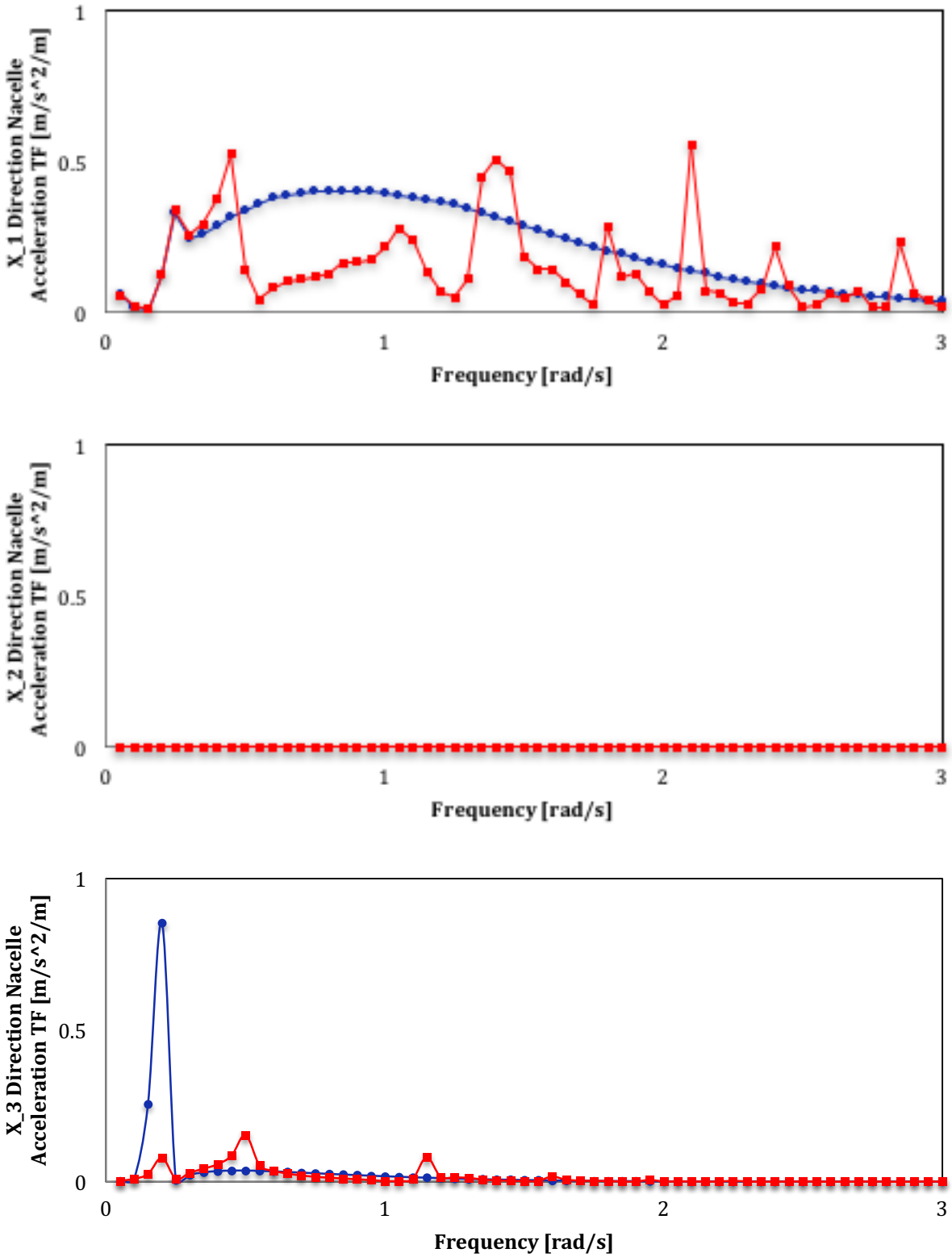

Figure 15. X_1-, X_2-, and X_3-direction Nacelle Accelerations for the Solitary Spar Floating Platform (Blue/Circle) and Body 1, S = 50m, Scenario (Red/Square)

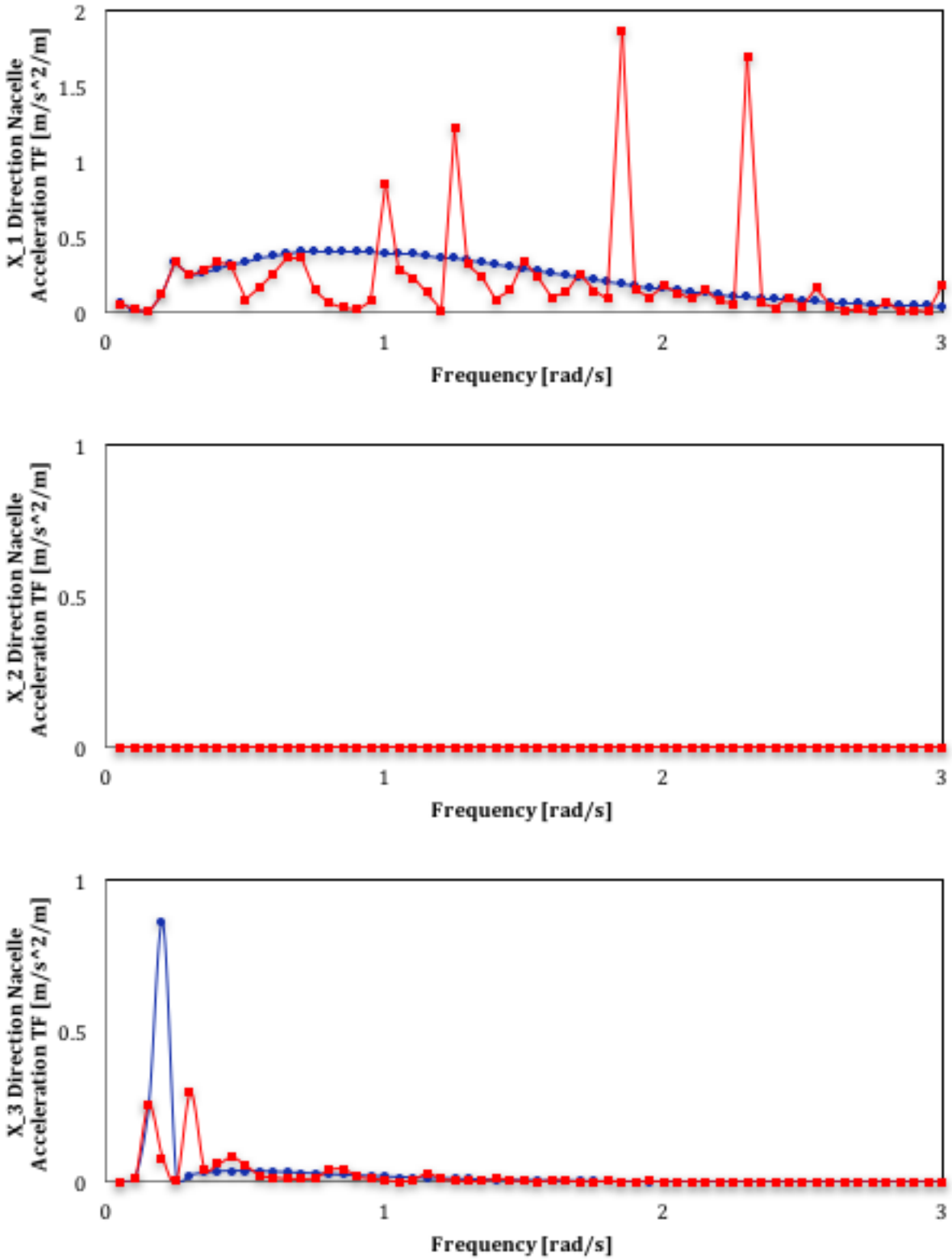

Figure 16. X_1-, X_2-, and X_3-direction Nacelle Accelerations for the Solitary Spar Floating Platform (Blue/Circle) and Body 1, S = 100m, Scenario (Red/Square)

Table 10. RMS Nacelle Acceleration Per Incident Wave Height and Percent Change for a Wave Bridge and Spar with S = 20 m

	X_1–Direction [m^2/s/m]/[%]	X_2–Direction [m^2/s/m]/[%]	X_3–Direction [m^2/s/m]/[%]	RMS Nacelle Acceleration/ Ψ [m^2/s/m]/[%]
Full Range of Wave Frequencies (0.05 – 3.00 rad/s)	0.2430 -4.66%	0.0000 0%	0.0345 -70.35%	0.1417 -21.85%
Normal Operating Range (0.80 - 2.00 rad/s)	0.2510 -20.04%	0.0000 0%	0.0107 -13.15%	0.1450 -20.03%
Rough Water Range (0.20 – 3.0 rad/s)	0.2492 -4.67%	0.0000 0%	0.0352 -69.23%	0.1453 -11.69%

Table 11. RMS Nacelle Acceleration Per Incident Wave Height and Percent Change for a Wave Bridge and Spar with S = 50 m

	X_1–Direction [m^2/s/m]/[%]	X_2–Direction [m^2/s/m]/[%]	X_3–Direction [m^2/s/m]/[%]	RMS Nacelle Acceleration/ Ψ [m^2/s/m]/[%]
Full Range of Wave Frequencies (0.05 – 3.00 rad/s)	0.2006 -21.32%	0.0000 0%	0.0312 -73.19%	0.1172 -27.55%
Normal Operating Range (0.80 - 2.00 rad/s)	0.2188 -30.29%	0.0000 0%	0.0181 47.05%	0.1267 -30.11%
Rough Water Range (0.20 – 3.0 rad/s)	0.2056 -21.34%	0.0000 0%	0.0318 -72.21%	0.1201 -27.08%

Table 12. RMS Nacelle Acceleration Per Incident Wave Height and Percent Change for a Wave Bridge and Spar with S = 100 m

	X_1–Direction [m^2/s/m]/[%]	X_2–Direction [m^2/s/m]/[%]	X_3–Direction [m^2/s/m]/[%]	RMS Nacelle Acceleration/ Ψ [m^2/s/m]/[%]
Full Range of Wave Frequencies (0.80 – 2.00 rad/s)	0.4137 62.27%	0.0000 0%	0.0545 -53.09%	0.2409 48.91%
Normal Operating Range (0.80 - 2.00 rad/s)	0.5056 61.08%	0.0000 0%	0.0147 19.39%	0.2920 61.03%
Rough Water Range (0.20 – 3.0 rad/s)	0.4243 62.31%	0.0000 0%	0.0448 -60.83%	0.2464 49.54%

The summary of the RMS nacelle accelerations and the percent change for each Wave Bridge and Spar scenario is shown in Table 10, Table 11, and Table 12. A negative percentage indicates a performance improvement as a result of the Wave Bridge and a positive percentage indicates a performance degradation as a result of the Wave Bridge. Table 10, Table 11, and Table 12 identify several characteristic.

First, the Wave Bridge induces the greatest effect on the x_1-direction acceleration when the frequency range is limited to the Normal Operating Range (0.80 – 2.00 rad/s) where 20.04% and 30.29% performance improvements can be seen for separations distance of 20m and 50m. As opposed to 4.67% and 4.66% performance improvements for the separation distance 20m Rough Water Range and Full Range and 21.34% and 21.32% performance improvements for the separation distance 50m Rough Water Range and Full Range. This is due to the very low magnitude pitch acceleration during the frequencies excluding the standing waves.

Second, the Wave Bridge induces the greatest effect on the x_1-direction acceleration when evaluating the Full Range. The performance improvement 70.35%, 73.19% and 53.09% for the separation distances of 20m, 50m, and 100m, respectively. This is dues to the heave acceleration dues to the natural frequency of the Spar at 0.2 rad/s that was eliminated due to the presence of the Wave Bridge.

Third, contribution of the heave acceleration is virtually insignificant because the magnitude of the pitch accelerations compared to the heave accelerations is significantly greater. This may guide future research in focusing on minimizing the floating platform rotations of roll and pitch instead of the evaluating all mode of motion.

Lastly, the Percent Relative RMS Nacelle Acceleration [Ψ] shows performance improvement for the scenarios involving the separation distances of 20m and 50m. However,

there is significant performance degradation for the separation distance of 100m, indicating an upper limit may exist for the separation distance dimension, between 50m and 100m, where there is no overall performance improvement.

The Effects of Incident Wave Angle and Separation Distance of the Wave Bridge Bodies on the Hydrodynamic Performance of the Spar Floating Platform (Study 2)

This study utilized Body 2 and varied the separation distance (20m, 40m, 60m, 80m, and 100m) and the incident wave angle (0, 45, and 90 degrees). Selected nacelle acceleration RAOs are shown in Figure 17, Figure 18, and Figure 19 for the case of 0 degrees, 45 degrees, and 90 degrees incident angles, respectively. The characteristics of the nacelle acceleration RAOs are similar throughout the range of separation differences; hence Figure 17, Figure 18, and Figure 19 are representative of the individual curves not shown. There are two important characteristic that must be explained.

First, there are standing waves present with in the sheltered zone at 0 degrees and 45 degrees. Hence, it can be surmised that there will be standing waves for any incident angle that contributes a wave component along the same axis as the Wave Bridge longitudinal centerline (i.e., all incident angles less than 90 degrees). However, the wave heights of these standing waves, and thereby their effects on pitch nacelle acceleration, are negatively correlated to the incident wave angle.

Second, the heave acceleration at the natural frequency of the Spar (0.2 rad/s) is damped for all incident wave angles. This reaction of the Spar is an intuitive reaction to the presence of a Wave Bridge at 0 degrees and 45 degrees incident wave angles. However, the reason for the damped RAOs at 90 degrees is unknown and must me further explored at a later time.

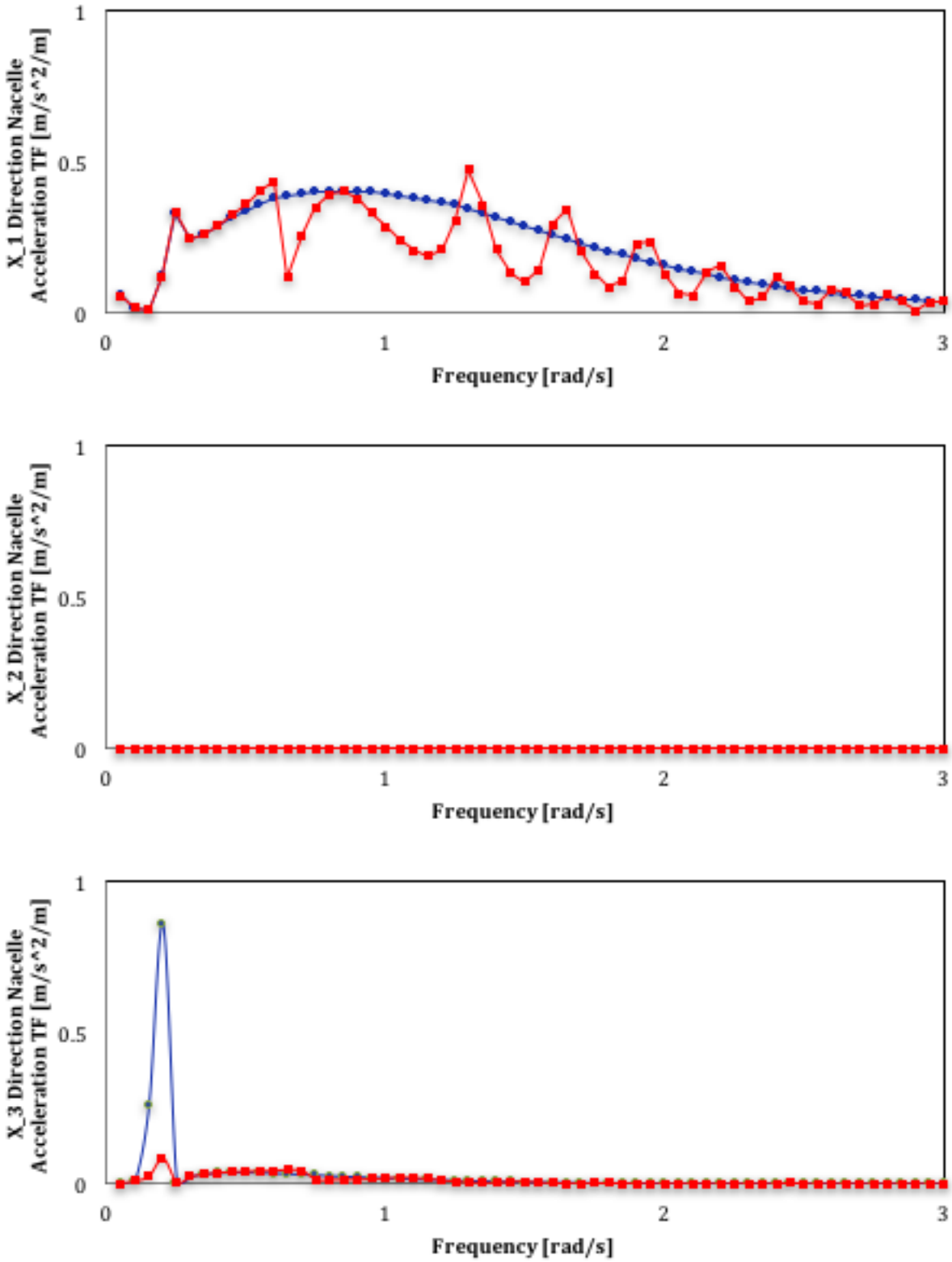

Figure 17. X_1-, X_2-, and X_3-direction Nacelle Accelerations for the Solitary Spar Floating Platform (Blue/Circle) and Body 2, D = 60m, 0 degrees Scenario (Red/Square)

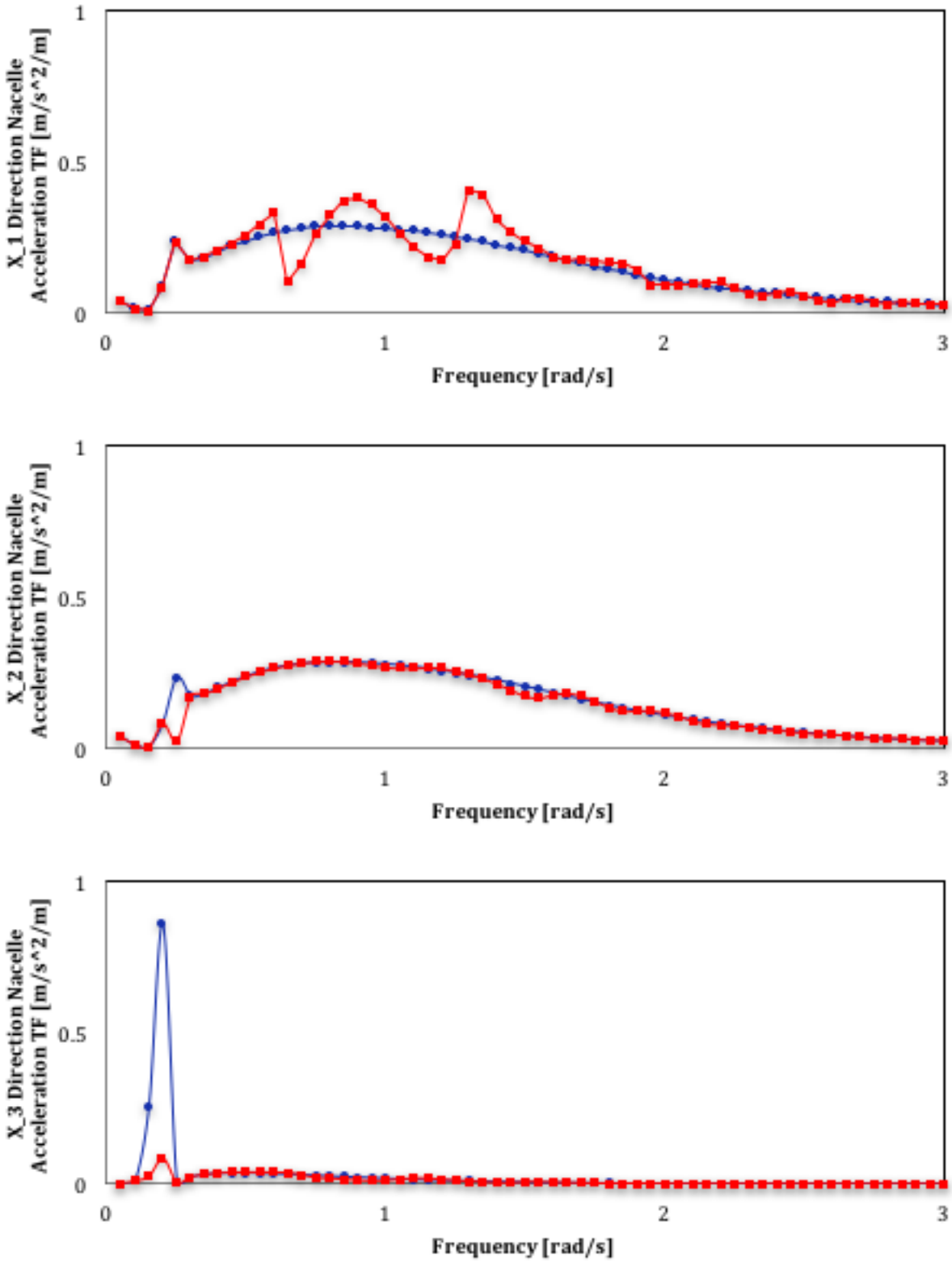

Figure 18. X_1-, X_2-, and X_3-direction Nacelle Accelerations for the Solitary Spar Floating Platform (Blue/Circle) and Body 2, D = 60m, 45 degrees Scenario (Red/Square)

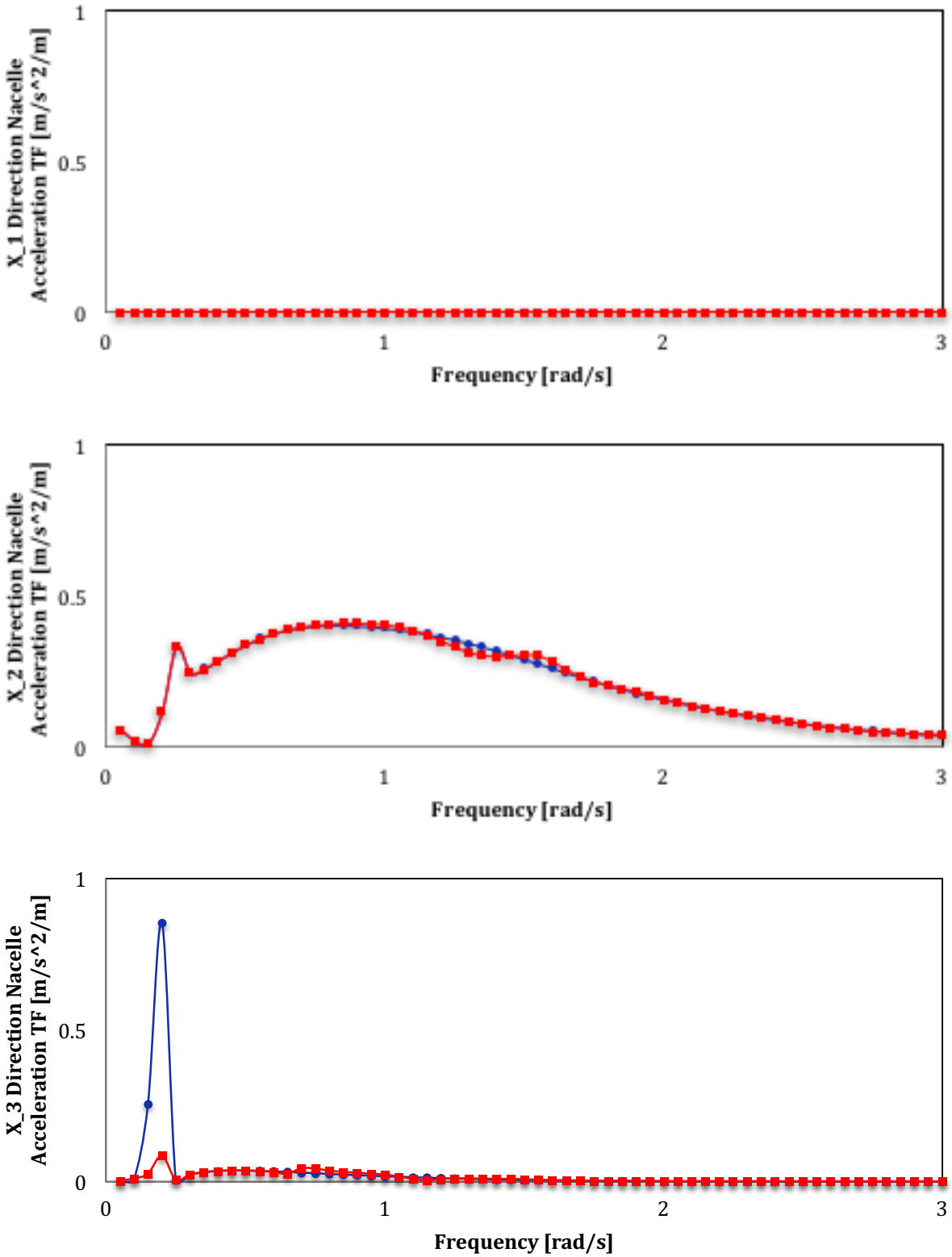

Figure 19. X_1-, X_2-, and X_3-direction Nacelle Accelerations for the Solitary Spar Floating Platform (Blue/Circle) and Body 2, D = 60m, 90 degrees Scenario (Red/Square)

Table 13. Percent Relative RMS Nacelle Acceleration, Ψ [%] for a Wave Bridge and Spar with Incident Wave Angle of 0 Degrees

	Separation Distance				
	20m	**40m**	**60m**	**80m**	**100m**
Full Range of Wave Frequencies (0.80 – 2.00 rad/s)	-15.27%	-18.85%	-19.84%	-19.42%	-19.22%
Normal Operating Range (0.80 - 2.00 rad/s)	-35.24%	-16.61%	-15.31%	-16.37%	-15.65%
Rough Water Range (0.20 – 3.0 rad/s)	-14.69%	-18.30%	-19.30%	-18.88%	-18.68%

Table 14. Percent Relative RMS Nacelle Acceleration, Ψ [%] for a Wave Bridge and Spar with Incident Wave Angle of 45 Degrees

	Separation Distance				
	20m	**40m**	**60m**	**80m**	**100m**
Full Range of Wave Frequencies (0.80 – 2.00 rad/s)	-1.55%	-5.34%	-5.50%	-3.88%	-3.69%
Normal Operating Range (0.80 - 2.00 rad/s)	2.69%	3.73%	7.57%	7.86%	7.09%
Rough Water Range (0.20 – 3.0 rad/s)	-0.87%	-5.78%	-4.85%	-3.22%	-3.02%

Table 15. Percent Relative RMS Nacelle Acceleration, Ψ [%] for a Wave Bridge and Spar with Incident Wave Angle of 0 Degrees

	Separation Distance				
	20m	**40m**	**60m**	**80m**	**100m**
Full Range of Wave Frequencies (0.80 – 2.00 rad/s)	-7.04%	-8.78%	-8.84%	-8.80%	-8.71%
Normal Operating Range (0.80 - 2.00 rad/s)	4.28%	0.24%	-0.06%	-0.15%	-0.06%
Rough Water Range (0.20 – 3.0 rad/s)	-6.39%	-8.15%	-8.21%	-8.17%	-8.08%

The summary of the Percent Relative RMS Nacelle Acceleration [Ψ] for each Wave Bridge and Spar scenario is shown in Table 13, Table 14, and Table 15. There are two items that agree with intuition. First, the 90 degree incident angle has virtually no effect on the Operational Range of the FWT. This agrees with intuition because to a certain extent the Spar behaves as if the Wave Bridge is not there. Second, the 45 degree incident angle reveals performance degradation. This agrees with intuition because the Spar no longer has a Wave Bridge body protecting the Spar but the Wave Bridge is still present and inducing standing waves further affect the Spar. Additionally, there are two characteristics, the body beam and the separation distance, that must be examined using the results of the first study.

The Percent Relative RMS Nacelle Acceleration, Ψ, of this study with Body 2 and the first study with Body 2 show the impact of the body volumes on the nacelle acceleration. This is contrary to intuition where one would expect a larger body on the Wave Bridge to create a protected region that is less likely to adversely affect the Spar. However, by examination of in Table 10 and Table 13 it is seen that for Body 1 performance degrades for a separation distance between 50m and 100m whereas performance improves for Body 2 throughout the range of separation distances, albeit a lower performance improvement for greater separation distances. This change in performance based on body volume is the result of the beam of the bodies. The beam of Body 1 (b = 74m) supports greater wave energy from the standing waves to affect the Spar. The beam on Body 2 (b = 20m) is only twice the width of the Spar hence the energy of standing waves affects the Spar to a lesser extent.

Additionally, the separation distance relative to the beam of the body is also a significant characteristic. Table 14 shows that the leading body of the Wave Bridge provides small, but quantifiable, magnitudes of performance improvement to the Spar at a separation distance of

20m and even less improvement at 40m. Conversely, Table 15 shows that the leading body of the Wave Bridge provides small, but quantifiable, magnitudes of performance degradation to the Spar at a separation distance of 20m and but less degradation at 40m. Table 10 and Table 13 show a difference aspect of this separation distance relation to beam. Table 10 indicates an upper limit may exist for the separation distance dimension for Body 1, between 50m and 100m, where there is no overall performance improvement and Table 13 indicates there is no upper limit for the separation distance for Body 2. Hence, the second aft body may not be beneficial to an optimized design.

Time Domain Visualization of the Wave Bridge

By inspection of the incident, diffraction, and radiation velocity potentials through the use of Neptune is it seen that the incident waves do not affect the sheltered region for much of the Operating Range. Visualization of the Wave Bridge shows wave fields within the sheltered region are either a result of the diffraction or radiation velocity potentials, parameters that are not related to the RAO data and can only be seen by inspection of the velocity potentials in Neptune.

The incident, diffracted, and radiated wave fields in the sheltered region are shown in Figure 20. The side view reveals the peaks and troughs of the waves. The scaling factor of the incident waves is 2. The evidence of standing waves is seen in the diffraction and radiation wave fields. Figure 20 shows diffracted waves of larger wave height than the incident waves. The radiated waves have a similar frequency than the diffracted waves, but the wave height is less. When these three wave fields are superimposed, Figure 21, the incident waves are seen outside of the sheltered region whereas the sheltered region has a standing waves along the centerline that are out of phase with the incident waves.

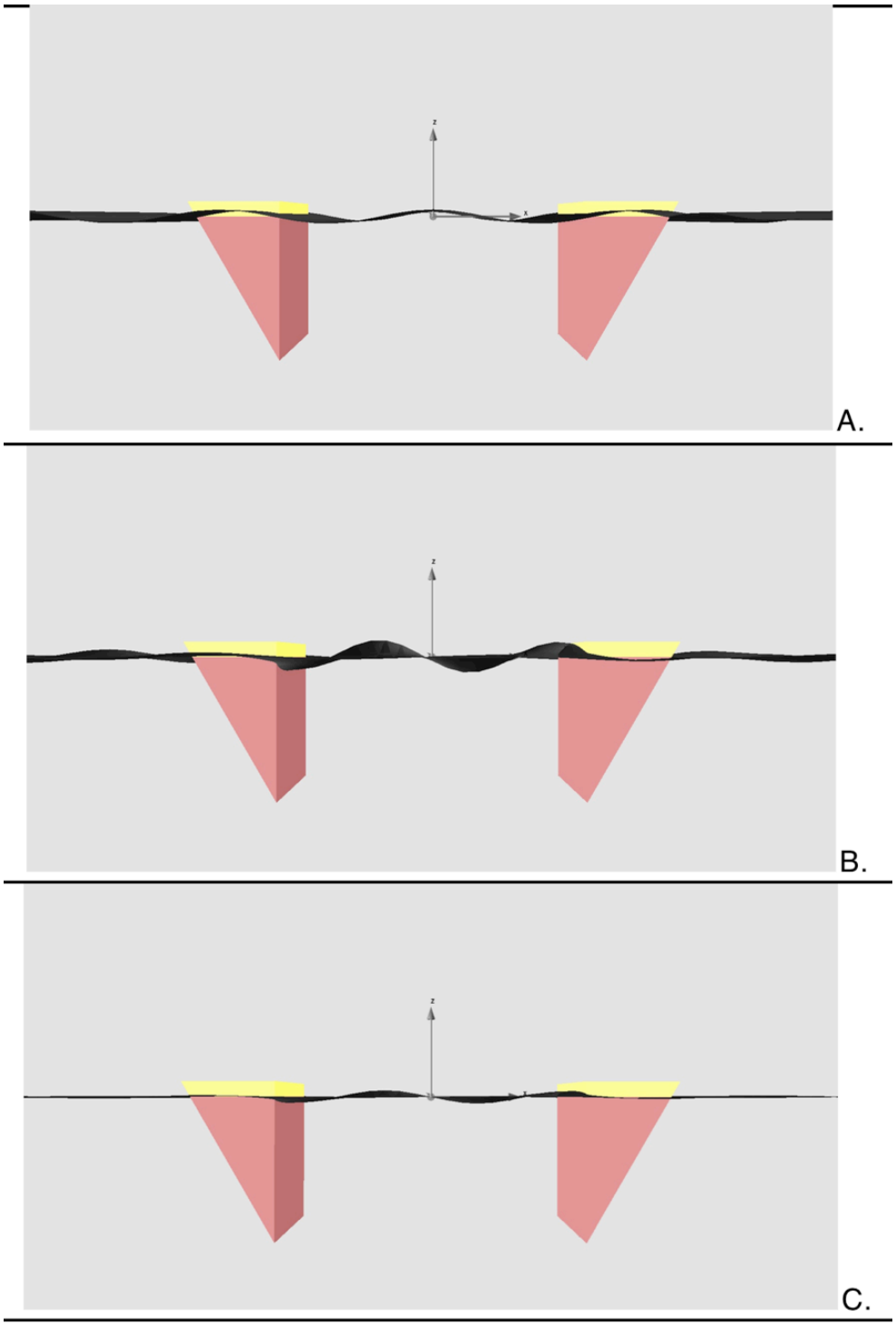

Figure 20. Neptune-generated time-domain wave field visualizations for waves with period, T=6.283 s (ω=1.0 rad/s). A) Incident waves, scaling factor = 2. B) Diffracted wave, scaling factor = 2. C) Radiated wave, scaling factor = 2.

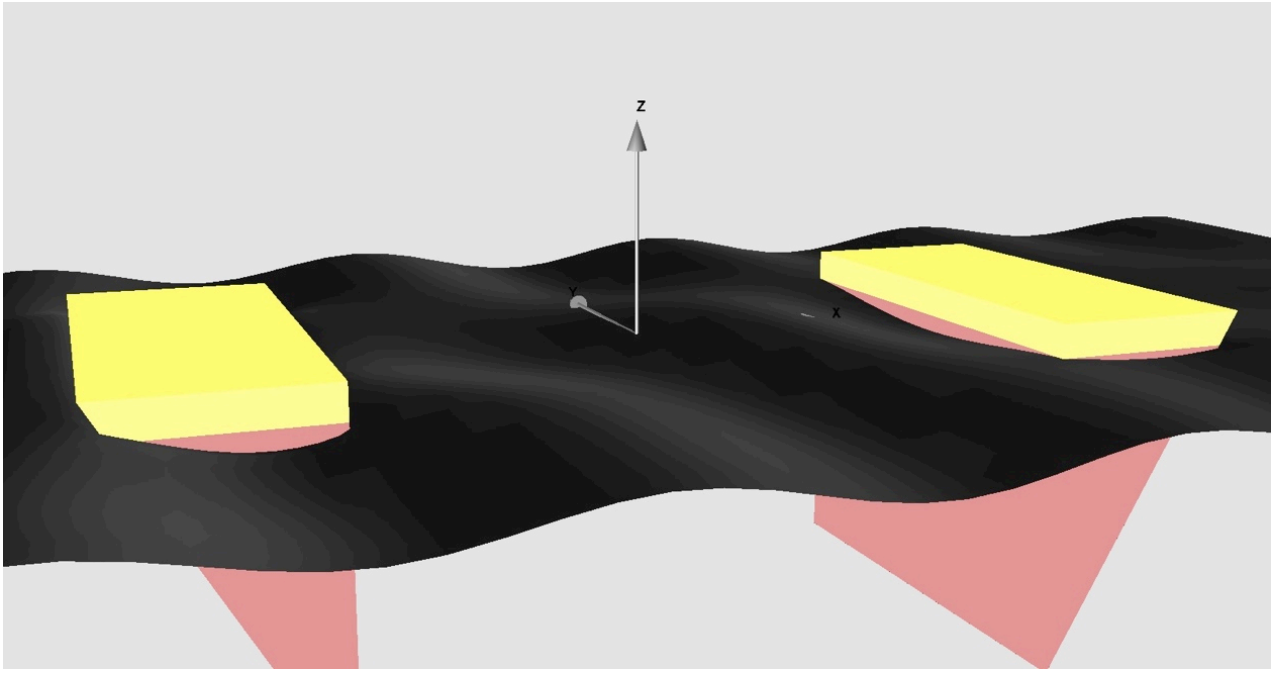

Figure 21. All wave fields superimposed

Chapter 7: Conclusion

The objective of the project was to determine the if performance improvement to the Spar could be obtained by the implementation of the Wave Bridge concept. Two bodies, Body 1 and Body 2, were the submerged volumes of the Wave Bridge. The separation distances of 20m, 50m, and 100m were evaluated for Body 1. The separation distances of 20m, 40m, 60m, 80m, and 100m and the incident wave angles of 0 degrees, 45 degrees, and 90 degrees were evaluated for Body 2. Performance was determined by the the nacelle acceleration. Performance improvement, - Ψ, and performance degradation, + Ψ, was determined for all scenarios.

Summary of the Spar

The case of the solitary Spar floating platform well defines the appropriate parameters of the hydrodynamic system and establishes the baseline upon which the Wave Bridge must show improvement in order to validate further research with such a concept. The spar floating platform is clearly a well-designed concept that can fare well on its own for a wide spectrum of waves. But, the Spar is susceptible to waves reacting in both the heave and pitch modes. The pitch mode of which is the dominant contributor to the nacelle acceleration and must be minimized by inclusion of the Wave Bridge.

Summary of Study 1

It is shown by the nacelle acceleration RAOs and visual inspection of the Neptune results the presence of the Wave Bridge induced diffracted and radiated standing waves whose magnitudes are of a significant order of magnitude that can lead to adverse effects on objects within the sheltered area. The creation of a standing wave is not necessarily a bad thing. Standing waves are well-known and further understanding of the Wave Bridge geometry will result is better manipulation of the standing waves encountered. The range of frequencies a

floating platform will encounter at a real site would determine the actual effects on the floating platform. Additionally, the manipulation of Wage Bridge geometry could lead to site specific optimized Wave Bridges that minimize waves within the sheltered area acting upon floating platforms in the case of FWTs or maximizing internal waves acting upon floating platforms in the case of Wave Energy Converters (WECs).

Summary of Study 2

It has been shown that for head quartering waves (i.e. incident wave angle is greater than 0 but less than 45), standing waves will be present within the sheltered region. It has also been shown that the beam of the Wave Bridge body and separation distance can protect the spar for certain combinations. Lastly, the studies of the Wave Bridge and Spar combination have yielded results to show a relation between the beam of the body, the separation distance, and the nacelle acceleration. Future research to quantify this relationship would further develop the understanding of this Wave Bridge Concept and the relevancy and effectiveness of the Wave Bridge's trailing body.

Outcomes

Three key aspects were discovered in pursuit of performance improvement. First, significant performance improvement is possible with use of the Wave Bridge concept with performance improvements of up to 30% for Body 1 and 35% Body 2 calculated. Second, it was determined that the Wave Bridge concept facilitates the the presence of standing waves within the sheltered region. A phenomenon not seen in previous works because previous computation and experimental domains were 2D. Lastly, it was determined that the trailing body of the Wave Bridge concept is not beneficial to an optimized design because the trailing body creates the enclosed sheltered region that facilities standing waves and only the leading body protects the

Spar for incident wave angles greater that 0 and less that 45 degrees. The objective of the thesis has been adequately satisfied by the outcomes of this thesis. Further research is needed to fully evaluate if the Wave Bridge concept is a worthwhile industrial pursuit, but, based on the outcomes of this research the Wave Bridge concept does not appear to provide the performance or economic benefits sought by a growing industry.

Future Directions

Additional research to optimize the design of a body that will protect FWTs will most likely result in a departure from the Wave Bridge concept. The outcomes of this research give further justification to (1) designs which implement floating breakwaters forward of FWTs to diminish unidirectional waves shown by the effectiveness of Body 1 to significantly dampen all non-standing wave frequencies; (2) to designs which implement a torus shaped body that surround a FWT and react to wave like a large-scale moonpool as it interacts with omni-directional wave fields shown by the significant effects diffracted waves around the Wave Bridge had upon the Spar; or (3) designs to add pitch dampers to the Spar as evidenced by the pitch mode's dominance over the other modes of motion. New research as a result of the outcomes of this research would be to evaluate using the Wave Bridge concept or similar two-body design to maximize the generation of standing waves for the use of WECs.

REFERENCES

Heronemus, W. E. "Pollution-Free Energy From Offshore Winds", 8th Annual Conference and Exposition Marine Technology Society, Washington D.C., September 11-13, 1972.

Bulder, B.H., Henderson, A., Huijsmans, R.H.M., Peeringa, J.M., Pierik, J.T.G., Snijders, E.J.B., van Hees, M.Th., Wijnants, G.H., and Wolf, M.J., "Floating Offshore Wind Turbines for Shallow Waters," Public Report 2002-CMC-R43, ECN, MARIN, MSC, Lagerwey the Windmaster, TNO, TUD.

Normark, B. and Nielsen, E.K., "Advanced power electronics for cable connection of offshore wind," Copenhagen Offshore Wind 2005.

Cordle, A., Jonkman, J., "State of the Art in Floating Wind Turbine Design Tools," 2011, Conference Paper NREL/CP-5000-50543.

Musial, W., Butterfield, S., Boone, A., "Feasibility of Floating Platform Systems for Wind Turbines," 2004, Conference Paper NREL/CP-500-34874.

Musial, W. and Butterfield, S., "Energy from Offshore Wind," 2006, Conference Paper NREL/CP-500-39450.

Sclavounos, P., Tracy, C., and Lee, S., "Floating Offshore Wind Turbines: Responses in a Seastate Pareto Optimal Designs and Economic Assessment," 2007.

Wu, Y.-C., "Plunger-type wavemaker theory," 1988, Journal of Hydraulic Research, Vol. 26, No. 4.

Mei, C. (1976). Power Extraction from Water Waves. Journal of Ship Research 20(2), 63-66.

Evans, D. (1976). A Theory for Wave-Power Absorption by Oscillating Bodies . Journal of Fluid Mechanics 77(1) , 1-25.

Newman, J. (1962). The Exciting Forces on Fixed Bodies in Waves. Journal of Ship Research, 10-17.

Newman, J. (1977). Marine Hydrodynamic. M.I.T Press.

Alam, R., “A Perfect Wave Energy Converter,“ 2010, Not Published.

Falnes, J. (2007). A Review of Wave Energy Extraction. Marine Structures 20, 185-201.

Ghorbani, R., Alam, R., Shakeri, M., “Dynamic Load Mitigation of a Floating Offshore Wind Turbine Station,” 2012, NSF Proposal, Not Published.

Jonkman, J., “Definition of the Floating System for Phase IV of the OC3,” 2010, Technical Report NREL/TP-500-47535.

Gueydon, S. and Xu, Wei, “Floating Wind Turbine Motion Assessment,” 2011, *OCEANS 2011* , vol., no., pp.1-10, 19-22 Sept. 2011.

MARIN, “DIFFRAC User Guide Version 2.4”, June 2011